Received: 17 June 2020 | Revised: 15 September 2020 | Accepted: 16 September 2020

DOI: 10.1111/jnc.15200

ORIGINAL ARTICLE

Journal of Neurochemistry JNC The Official Journal of the International Society for Neurochemistry WILEY

Olfactory bulb-targeted quantum dot (QD) bioconjugate and Kv1.3 blocking peptide improve metabolic health in obese male mice

Austin B. Schwartz[1] | Anshika Kapur[2] | Zhenbo Huang[3,4] | Raveendra Anangi[5] | John M. Spear[2,5] | Scott Stagg[2,5] | Erminia Fardone[3] | Zolan Dekan[5] | Jens T. Rosenberg[6] | Samuel C. Grant[6,7] | Glenn F. King[5] | Hedi Mattoussi[2] | Debra Ann Fadool[1,3,4]

[1]Institute of Molecular Biophysics, The Florida State University, Tallahassee, FL, USA

[2]Department of Chemistry and Biochemistry, The Florida State University, Tallahassee, FL, USA

[3]Program in Neuroscience, The Florida State University, Tallahassee, FL, USA

[4]Department of Biological Science, The Florida State University, Tallahassee, FL, USA

[5]Institute for Molecular Bioscience, The University of Queensland, Brisbane, Qld, Australia

[6]National High Field Magnetic Laboratory, The Florida State University, Tallahassee, FL, USA

[7]Department of Chemical & Biomedical Engineering, FAMU-FSU College of Engineering, Florida State University, Tallahassee, FL, USA

Correspondence
Debra Ann Fadool, 319 Stadium Drive, KIN Life Science Building, Program in Neuroscience & Institute of Molecular Biophysics, Florida State University, Tallahassee FL 32306, USA.
Email: dfadool@bio.fsu.edu

Funding information
National Science Foundation (NSF), Grant/Award Number: DMR-1644779, 1508501 and 1613988; State of Florida;

Abstract

The olfactory system is a driver of feeding behavior, whereby olfactory acuity is modulated by the metabolic state of the individual. The excitability of the major output neurons of the olfactory bulb (OB) can be modulated through targeting a voltage-dependent potassium channel, Kv1.3, which responds to changes in metabolic factors such as insulin, glucose, and glucagon-like peptide-1. Because gene-targeted deletion or inhibition of Kv1.3 in the periphery has been found to increase energy metabolism and decrease body weight, we hypothesized that inhibition of Kv1.3 selectively in the OB could enhance excitability of the output neurons to evoke changes in energy homeostasis. We thereby employed metal-histidine coordination to self-assemble the Kv1.3 inhibitor margatoxin (MgTx) to fluorescent quantum dots (QDMgTx) as a means to label cells in vivo and test changes in neuronal excitability and metabolism when delivered to the OB. Using patch-clamp electrophysiology to measure Kv1.3 properties in heterologously expressed cells and native mitral cells in OB slices, we found that QDMgTx had a fast rate of inhibition, but with a reduced $IC_{50,}$ and increased action potential firing frequency. QDMgTx was capable of labeling cloned Kv1.3 channels but was not visible when delivered to native Kv1.3 in the OB. Diet-induced obese mice were observed to reduce body weight and clear glucose more quickly following osmotic mini-pump delivery of QDMgTx/MgTx to the OB, and following MgTx delivery, they increased the use of fats as fuels (reduced respiratory exchange ratio). These results suggest that enhanced excitability of bulbar output neurons can drive metabolic responses.

Abbreviations: ACSF, ANOVA, analysis of variance; BSA, bovine serum albumin; cDNA, copy DNA; CLAMS, Comprehensive Laboratory Animal Metabolic System; Da, dalton; DAPI, 4′,6-diamidino-2-phenylindole; DIO, diet-induced obesity; EE, energy expenditure; FBS, fetal bovine serum; GLP-1, glucagon-like peptide 1; HEK293 cells, human embryonic kidney 293 cells; HisMgTx, histidine epitope-tagged margatoxin; HPLC, high-performance liquid chromatography; iAUC, integrated area under the curve; I_I, initial current; I_n, current at the nth pulse; IND, intranasal delivery; IPGTT, intraperitoneal glucose tolerance test; IPI, interpulse interval; Kv1.3, voltage-dependent potassium channel 1.3; Kv1.3$^{-/-}$, global knockout of Kv1.3; MgTx, margatoxin; MRI, magnetic resonance imaging; OB, olfactory bulb; OSNs, olfactory sensory neurons; P, post-natal day; PBS, phosphate-buffered saline; P_d, pulse duration; PEG, polyethylene glycol; PFA, paraformaldehyde; pI, isoelectric point; QD, quantum dot; QDMgTx, quantum dot margatoxin conjugate; RER, respiratory exchange ratio; RM, repeated measure; RRID, Research Resource Identifier; RT, room temperature; *SEM*, standard error of the mean; *T*, time; *Vc*, command voltage; VCO2, volume of carbon dioxide produced through metabolism; VO2, volume of oxygen consumed.

National Institute on Deafness and other Communication Disorders (NIDCD), Grant/Award Number: R01DC013080, T32DC000044 and F31DC014638; FSU Legacy Fellowship; Robinson Endowment Award from Tallahassee Memorial Hospital; Stanley and Shirley Marshall Endowment Fund; Australian National Health & Medical Research Council, Grant/Award Number: APP1136889

KEYWORDS

margatoxin, metabolism, obesity, olfaction, potassium channel, RER

1 | INTRODUCTION

The olfactory bulb (OB) processes olfactory information relayed peripherally from the main olfactory epithelium to communicate to the brain concerning the external chemical environment cued by odorant molecules (Kleene, 2008; Antunes *et al*., 2014). The integrity of that information can be altered depending upon the nutritional state of the animal or individual, whereby fasting or excess nutrition can modify electrical signaling or the olfactory sensory structures in the OB (Aime *et al*., 2014; Fadool & Kolling, 2020; Julliard *et al*., 2017; Palouzier-Paulignan *et al*., 2012; Thiebaud *et al*., 2014). One of the drivers of excitability in the major projection neurons of the OB, the mitral cells, is a voltage-gated potassium channel, Kv1.3. Action potential firing frequency, shape, and spike train periodicity are known to be driven by metabolic hormones and important energy factors that decrease Kv1.3 current amplitude, suggesting that the ion channel can differentially regulate excitability based on nutritional status and energy homeostasis (Fadool & Kolling, 2020; Fadool *et al*., 2000, 2011; Julliard *et al*., 2017; Kovach *et al*., 2016; Marks & Fadool, 2007; Marks *et al*., 2009; Palouzier-Paulignan *et al*., 2012; Thiebaud *et al*., 2016, 2019; Tucker *et al*., 2010a; Tucker *et al*., 2010b; Tucker *et al*., 2013). Global gene-targeted deletion of Kv1.3 channel or pharmacological block of the channel peripherally in mice decreases body weight and reduces diet-induced obesity (DIO) (Fadool *et al*., 2004; Tucker *et al*., 2008, 2012a, 2012b; Upadhyay *et al*., 2013; Xu *et al*., 2003). Herein, our goal was to design a chemical probe to block Kv1.3 specifically in the OB, to determine if mice made obese through diet could lose body weight by changing excitability centrally.

We selected the pore-blocker margatoxin (MgTx) to inhibit Kv1.3 current flow and label cells expressing the channel because of its reported selectivity (Garcia *et al*., 1997; Garcia-Calvo *et al*., 1993; Knaus *et al*., 1995) and applications in the OB (Colley *et al*., 2004; Fadool & Levitan, 1998; Mast & Fadool, 2012; Schwartz *et al*., 2017). Luminescent quantum dots (QDs) were utilized because of their intense photo-properties and ability to tune their interactions with biomolecules via modification of the QDs polymer ligand (Sundberg & Bruce Martin, 1974; Wang *et al*., 2016). QDs have unique optical and spectroscopic properties (Mattoussi *et al*., 2012; Medintz *et al*., 2005) that make them advantageous drug vectors for bioimaging. MgTx can be covalently conjugated to polyethyleneglycol-modified Zn^{2+} QDs and still retain ability to inhibit Kv1.3 (Schwartz *et al*., 2017), so that the conjugated molecule can be visually tracked in vivo. However, controlling the valence and orientation of MgTx on the conjugates is difficult via this strategy (Mout *et al*., 2012), and significant loss of material during the conjugation limits in vivo applications (Schwartz *et al*., 2017). We have now, alternatively, produced recombinant MgTx with an N-terminal polyhistidine tag that allows self-assembly of a controlled number of peptides per QD. This approach has previously been reported to allow conjugation of a variety of biomolecules to both QDs and gold nanoparticles and can be attributed to the strong affinity of histidine for metal-rich surfaces (Aldeek *et al*., 2013a; Aldeek *et al*., 2013b; Anikeeva *et al*., 2006; Goldman *et al*., 2005a; Goldman *et al*., 2005; Medintz *et al*., 2006; Medintz *et al*., 2006; Sapsford *et al*., 2007; Sundberg & Martin, 1974; Wang *et al*., 2015a; Wang *et al*., 2016b). Compared to covalent conjugation, self-assembly driven by metal-His coordination is highly efficient and prevents significant loss of material while providing control over the number and orientation of biomolecules bound to the QD surface (Anikeeva *et al*., 2006; Goldman *et al*., 2005a; Goldman *et al*., 2005b; Medintz *et al*., 2006a; Medintz *et al*., 2003, 2004; Medintz *et al*., 2006b; Wang *et al*., 2007, 2016a).

Following production of MgTx with an N-terminal polyhistidine tag (HisMgTx) and conjugation of this peptide to QDs using polyhistidine self-assembly (QDMgTx), we electrophysiologically measured the bioconjugate's ability to inhibit Kv1.3 in a heterologous expression system. We then tested its ability to increase excitability by blocking the native channel in mitral cell neurons of the OB. Owing to our ability to synthesize the bioconjugate in sufficient quantity for in vivo applications, we delivered HisMgTx and QDMgTx to DIO mice using osmotic mini-pumps cannulated into the OB such that we could measure the ability of the inhibitor to modulate whole-body metabolism and confirm targeted inhibition of Kv1.3 in the OB. Block of Kv1.3 in the OB in the obese mice caused a reduction in body weight, modified fuel utilization, and altered ingestive behaviors. These results provide evidence that modulating OB physiology, centrally, through targeting Kv1.3 in the brain can change energy utilization and eating behaviors.

2 | MATERIALS AND METHODS

Our study design was not pre-registered as a clinical trial.

2.1 | Ethical approval

All animal experiments were approved by the Florida State University (FSU) Institutional Animal Care and Use Committee (IACUC) under

protocol #1427 and were conducted in accordance with the American Veterinary Medicine Association (AVMA) and the National Institutes of Health (NIH) guidelines. For preparation of OB slices, mice were anaesthetized with isoflurane (Aerrane; Baxter) using the IACUC-approved drop method and were then killed by decapitation (AVMA Guidelines on Euthanasia, June 2007).

2.2 | Animal care

All mice (C57BL/6J background strain, Research Resource Identifier, RRID:IMSR_JAX:000644; The Jackson Laboratory) were housed individually in conventional style open cages at the Florida State University *vivarium* on a standard 12/12 hr light/dark cycle and were allowed ad libitum access to 5,001 Purina Chow (Purina) or a moderately high fat diet (MHF, Cat. #D12266B, Research Diets, 32% fat, 17% protein, and 51% carbohydrate) and water. Because of need for metabolic assessment and surgical recovery, all mice were individually housed and provided with two sources of enrichment—a house and a nestlet. Post-natal day (P) 15–30 mice of both sexes were used for electrophysiology. Mice that were used for metabolic assessment were maintained on MHF diet upon weaning (P24) for an average of 7.5 to 8 months that was not significantly different between treatment groups (Control = 240 ± 20 days, MgTx = 232 ± 19 days, and QDMgTx = 232 ± 21 days; one-way ANOVA, $F(2,19) = 0.01547$, $p = .9847$). Assignment of animals to a treatment group was arbitrary and the mean body weight for a treatment group following induction of obesity and prior to surgery was not significantly different (Control = 37.0 ± 1.6 g, MgTx = 35.1 ± 1.5 g, and QDMgTx = 39.2 ± 1.7 g; one-way ANOVA, $F(2,19) = 1.411$, $p = .2682$). Because experiments were designed to test the metabolic effect of QD conjugates following diet-induced obesity, only male mice were used in these studies given our previous report that female mice do not gain adiposity or body weight (Tortoriello *et al*., 2004, 2007). A total of 55 mice were used in our study. Our experiments were exploratory and the study design did not contain pre-determined exclusion criteria. Four mice were excluded in the study's results (one was excluded as a statistical outlier (two-sided Grubbs' test), two developed dermatitis as a result of oily fat diet, and one did not survive surgery) and an additional five mice were used to optimize placement of the osmotic minipump using stereotactically guided surgery. The number of subjects per experiment is specified in the figures and figure legends. Animal subjects were not randomized, rather assignment of animals to a treatment group was arbitrary—the surgeon blindly selected which pump to implant while a separate investigator loaded and retained the knowledge of pump contents. Each of the pumps (phosphate-buffered saline [PBS] control, HisMgTx, and QDMgTx) had an equal chance of being selected. Animals were metabolically screened in cohort sizes of four because this number of surgeries was achievable in a day's duration. Each day contained mouse surgery using all treatment groups so that data collection was not biased.

2.3 | Solutions and reagents

All salts and sugars were purchased from Sigma-Aldrich or ThermoFisher Scientific. Solutions used for expression and purification of the His-conjugated margatoxin peptide (HisMgTx) included Luria broth (LB, Cat. #244620; BD Biosciences) supplemented with 1% glucose, 0.5 M isopropyl β-D-1-thiogalactopyranoside (IPTG, #5800; EM Science), equilibration buffer (25 mM Tris, 300 mM NaCl), 50 mM EDTA, 100 mM $NiSO_4$, and 300 mM imidazole. PBS was used for conjugation (pH 8.0), prepared as previously described (Biju *et al*., 2008). For whole-cell electrophysiology experiments using human embryonic kidney 293 cells (HEK293 cells), the bath solution consisted of (in mM): 150 NaCl, 5 KCl, 2.6 $CaCl_2$, 2 $MgCl_2$, and 10 Hepes, pH 7.4; 305 milliosmole (mOsm). The intracellular pipette solution consisted of (in mM): 145 KCl, 10 HEPES, 10 EGTA, 2 $MgCl_2$, 3 NaATP, 0.4 GTP, pH7.4; 295 mOsm. The artificial cerebrospinal fluid (ACSF), sucrose-modified ACSF, and intracellular pipette solution for slice electrophysiology experiments were carefully monitored for osmolarity and prepared as previously reported (Fadool *et al*., 2011; Tucker et al. 2013; Thiebaud *et al*., 2016).

2.4 | cDNA constructs

All *Shaker* channel coding regions were downstream from a cytomegalovirus promoter. Rat Kv1.3 (rKv1.3) was subcloned into the multiple cloning region of $pcDNA_3$ (now available only as 3.1; RRID:Addgene_23252; originally 3.0 Invitrogen) at the unique *Hind*III restriction site as previously described (Holmes *et al*., 1996). DNA encoding human CD8 was amplified from pCDM8 (RRID:Addgene_11588) and subcloned into the $pcDNA_3$ vector between the *Bam*H1 and *Eco*R1 restriction sites (Mast *et al*., 2010). DNA encoding MgTx was subcloned into a PET-28b vector (Cat. # 69865-3; EMD Biosciences) containing a His_6 tag on the N-terminus.

2.5 | Experiment 1. Quantum dot (QD) synthesis and conjugation to margatoxin (MgTx)

2.5.1 | QD growth and phase transfer

The luminescent CdSe-ZnS core-shell quantum dots (QDs) used in this study had an approximate diameter of 6 nm and emitted in the green region of the visible spectrum (peak at 533 nm) (Clapp *et al*., 2006; Yu & Peng, 2002). These nanocrystals were grown stepwise, starting with the core, followed by ZnS overcoating, using high-temperature reduction of cadmium, selenium, zinc, and sulfur precursors in coordinating solvent mixtures made of alkylphosphines, alkyphosphine-carboxyl, and alkylamines, following previous protocols (Clapp *et al*., 2006). The native capping ligands, made of a mixture that included trioctylphosphine/triocylphosphineoxide (TOP/TOPO) and alkylphosphonic acid, were exchanged with poly(isobutylene-*alt*-maleic anhydride)

(PIMA)-based polymer ligand presenting several imidazole and zwitterionic moieties (His-PIMA-ZW) to promote dispersion of the QDs in buffer media and allow conjugation to His-biomolecules. Additional details on the phase transfer, conjugation steps, and purification of the conjugates can be found in previous reports (Wang *et al*., 2016; Wang *et al*., 2015). The final concentration of the QD dispersion was determined from the absorbance at 350 nm, using an extinction coefficient of 2.467×10^{-6} $M^{-1}cm^{-1}$ for the QDs (Leatherdale *et al*., 2002).

2.5.2 | Recombinant expression of HisMgTx

His-conjugated margatoxin (HisMgTx) was subcloned into the multiple cloning region of the pET-28b+ vector (EMD Biosciences, Cat. #69865-3) using *Nde*I and *Xho*I restriction sites (Addgene Vector Database). The construct was transformed into BL21 SHuffle T7 Express *Escherichia coli* (New England BioLabs, Cat.#C3029J). The pET-28b vector included an N-terminal His_6 tag, which allowed for affinity purification and conjugation to QDs and a thrombin cleavage site (underlined) between the His_6 tag and the MgTx coding sequence (MGSSHHHHHH-SSGLVPRGS-HMTIINVKCTSPKQCLP PCKAQ FGQSAGAKCMNGKCKCYPH). BL21 SHuffle T7 Express *E. coli* contain an oxidizing cytoplasm that promotes proper disulfide bond formation in HisMgTx. Transformed *E. coli* were grown in LB with 1% glucose at 37°C to OD_{600} = 0.8 while shaking at 250 RPM, then expression was induced with 0.5 mM IPTG at 16°C while shaking at 250 RPM (Figure 1a). Following overnight expression, bacterial cells were lysed using a microfluidizer (110L; Microfluidics), then HisMgTx was purified from the clarified lysate using nickel affinity chromatography (Gold Biotechnology, #H-320-50) followed by reversed-phase high-performance liquid chromatography (RP-HPLC), as shown in Figure 1b. RP-HPLC (Shimadzu Prominence HPLC) was performed with a C_{18} analytical column (Cat. #651286-8; Phenomenex) using a flow rate of 1 ml/min and a gradient of 15%–30% solvent B (0.075% trifluoroacetic acid (TFA) in 90% acetonitrile) in solvent A (0.1% TFA in water) over 50 min. HisMgTx was detected using the peptide absorbance at 220 nm. The monoisotopic mass of the purified recombinant HisMgTx determined using mass spectrometry was 6,475.9 kDa (Figure 1c). The purified HisMgTx was quantified using a Qubit Fluorimeter (Model #Q32857; ThermoFisher Scientific), then lyophilized (Model #MODULYOD-115; ThermoFisher Scientific) and stored at −20°C. Prior to use, the peptide was reconstituted in PBS with 0.05% bovine serum albumin (BSA).

2.5.3 | Preparation of QDMgTx

HisMgTx was conjugated to QDs (referred to as QDMgTx) by mixing the peptide with His-PIMA-ZW capped QDs in PBS followed by incubation at 4°C for 1 hr. Addition of the His_6 tag to

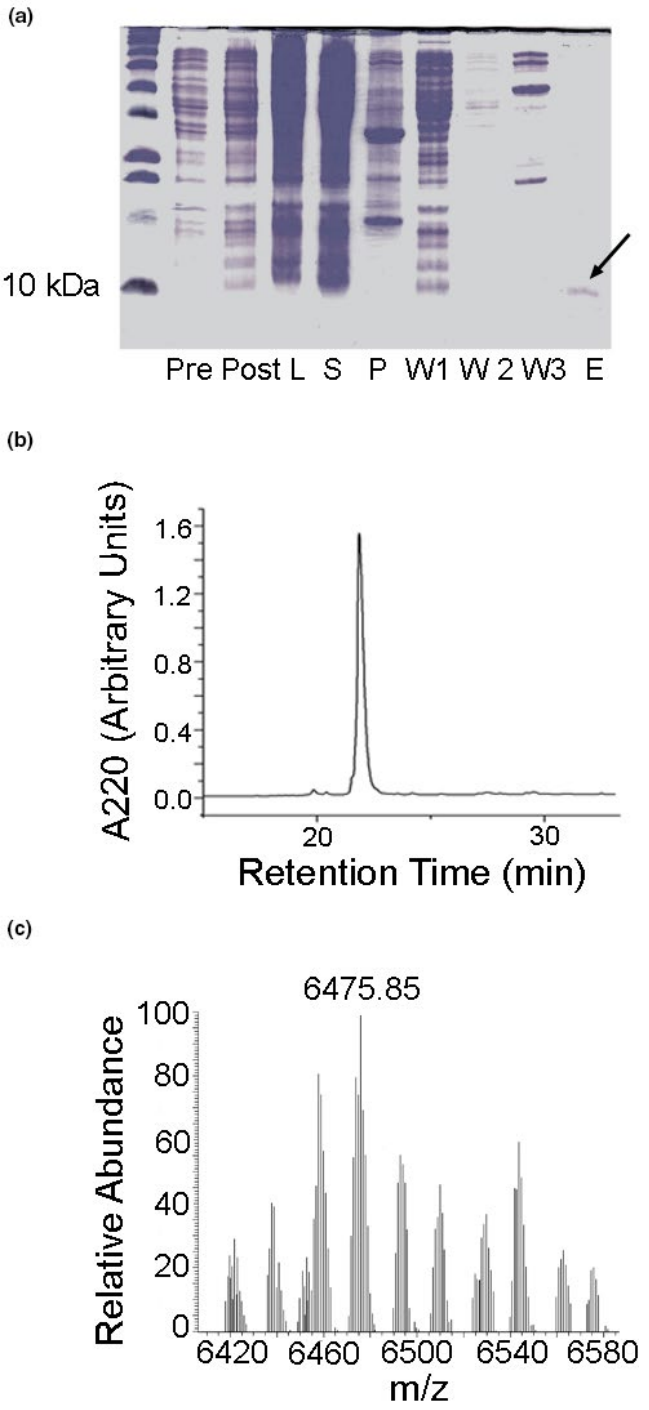

FIGURE 1 Purification of HisMgTx from T7 Shuffle Express *E. coli*. (a) 20% acrylamide gel illustrating various stages in the expression and purification of recombinant HisMgTx. Pre = pre-induction sample, Post = post-induction sample, L = cell lysate, S = supernatant, P = pellet, W1 = wash 1 from affinity column, W2 = wash 2 from affinity column, E = elution with 50 mM imidazole. Arrow = eluted protein product. (b) Reversed-phase high-performance liquid chromato (RP-HPLC) chromatogram with single peak at ~23 min retention time corresponding to recombinant HisMgTx. (c) LC-MS/MS spectrum of purified HisMgTx, showing a monoisotopic mass of 6,475.85 Da. HisMgTx, histidine epitope-tagged margatoxin

the N-terminus of MgTx allowed facile binding to Zn^{2+} as a result of high affinity of histidine for Zn^{2+}. Altered electrophoretic mobility of QDMgTx in comparison to non-conjugated QDs on a 0.8% agarose gel confirmed successful interaction of HisMgTx with the QDs (Figure 2). For the agarose gel experiments, several QDMgTx dispersions were prepared where the molar ratio of QD:HisMgTx varied from 1:10 to 1:60. QD concentration was maintained at 100 nM. For all cell labeling, electrophysiology, and animal studies, the QDMgTx was prepared at molar ratio of 1:15 and concentrations described for QDMgTx are with respect to the QD.

2.6 | Experiment 2. Using heterologously expressed Kv1.3 channels to test QD targeting and function

2.6.1 | Maintenance and transfection of HEK293 cells

We used Human Embryonic Kidney Cells (HEK293; RRID:CVCL_0045) that are not listed as a commonly misidentified cell line at the International Cell Line Authentication Committee Registry (ICLACR). Our HEK293 cells were contributed by Dr. Robert Margolski (Monell Chemical Senses Center) and have been authenticated for cross-contamination and misidentification by profiling short tandem repeats. Moreover, cell culture practices at Florida State University have followed "Guidance on Good Cell Culture Practices (GCCP)" (Coecke *et al.*, 2005). Our last cryopreserved batch of HEK293 cells was prepared in February of 2016 and each vial is experimentally used between passages 4 and 25. HEK293 cells were grown in Modified Eagle's Medium (MEM, Cat. #12360-038; ThermoFisher Scientific/Gibco) supplemented with 2% penicillin/streptomycin (Cat. #P0781; Sigma) and 10% fetal bovine serum (Cat. #16000-044; ThermoFisher Scientific/Gibco). Plating to low density and transfection procedures were as previously described (Cook & Fadool, 2002). Briefly, when cells reached 70%–80% confluency they were transiently co-transfected with 0.3 μg Kv1.3 and 0.2 μg pCDM8 cDNAs for 4 hr using lipofectamine (Cat. #18324-012; ThermoFisher Scientific/Invitrogen) in serum-reduced media (OptiMEM, Cat. #31985-070; ThermoFisher Scientific/Gibco). Including cDNA encoding the human CD8 transmembrane protein permitted panning for transfected cells by labeling cells with a red polypropylene antibody-linked bead prior to patch clamping (Mast & Fadool, 2012). The investigator was not blind to which cDNA was transfected into the HEK 293 cells.

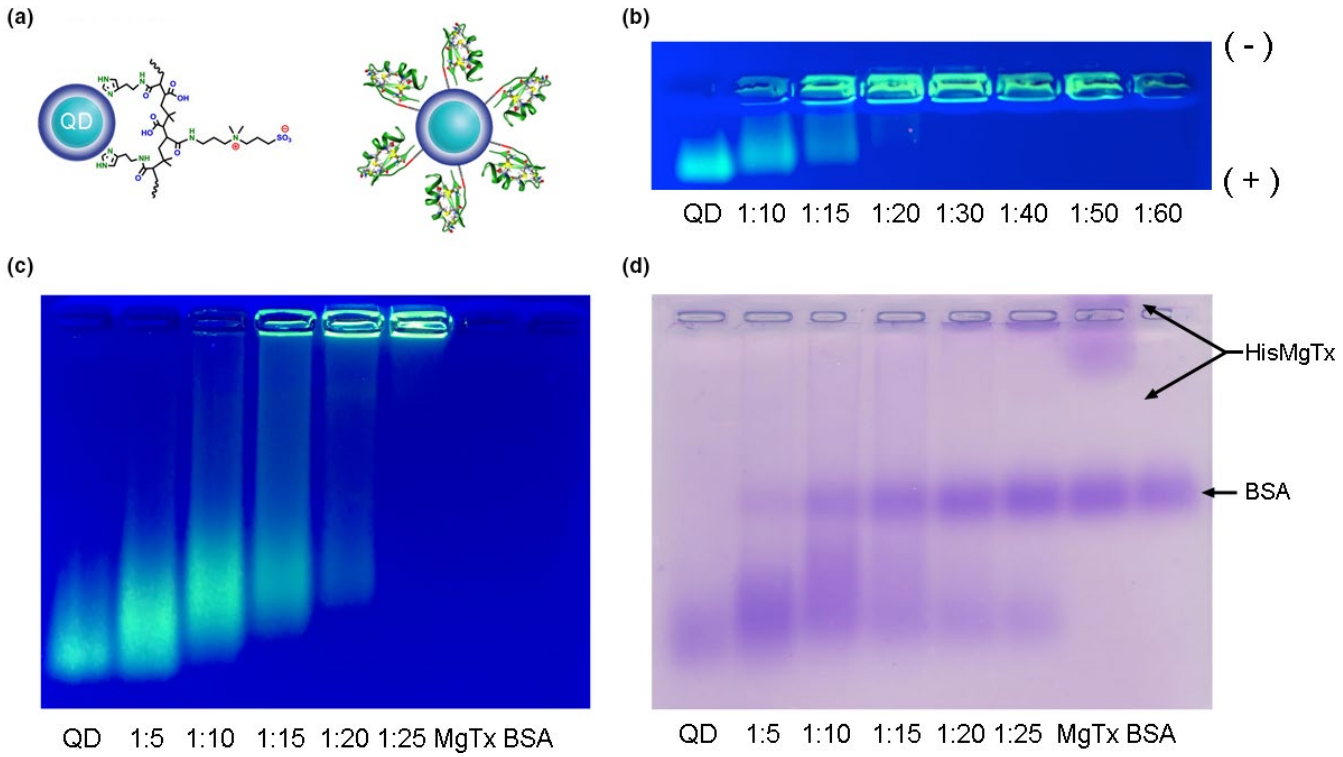

FIGURE 2 Conjugation of HisMgTx to green CdSe-ZnS core-shell quantum dots (QDs). These QDs were modified with a polyimidazole-based zwitterionic ligand containing the short-chain poly(isobutylene-*alt*-maleic anhydride) (His-PIMA-ZW). (a) Schematic representation of a QD modified with His-PIMA-ZW (Wang *et al.*, 2016) and of the same QD with HisMgTx bound to its surface. (b) 0.8% agarose gel confirming HisMgTx binding to QDs (20 min run time). As a larger ratio of HisMgTx is bound to the surface, the constructs' mass increases. [QD] =100 nM. (+) and (−) indicate positive and negative poles of gel. (c) Same as (b), however, the sample was electrophoresed for longer (70 min) and includes HisMgTx (MgTx = HisMgTx) and bovine serum albumin (BSA) (carrier protein for HisMgTx). (d) Coomassie stain of (c), to probe the presence of peptide not bound to QDs following conjugation (MgTx = HisMgTx)

2.6.2 | Electrophysiology of HEK293 cells

Thirty-six hours post-transfection, cells were incubated with Dynabeads® CD8 microparticles (Cat. #11147D; Thermo Fisher Scientific/Gibco) for 2 min to visualize channel-transfected cells (Mast & Fadool, 2012). Hoffman modulation contrast optics was used to visualize cells at 40 × magnification (Axiovert 135; Carl Zeiss). Patch electrodes were fabricated from Sutter glass (BF150-86-15; Sutter Instrument Co.) using a vertical puller (Model PP-830; Narishige) to achieve pipette resistances of 7–10 MΩ. Outward currents were recorded at room temperature (RT; 20–22°C) as acquired from the whole-cell configuration using an Axopatch 200B patch-clamp amplifier (Molecular Devices/Axon Instruments). All voltage signals were generated and data acquired with the use of an Axon Digidata 1,200 A/D converter in conjunction with pClamp v10.3 software (Molecular Devices/Axon Instruments). Recordings were filtered at 2 kHz and digitized at 2–5 kHz. Typically, cells were held (V_h) at − 90 mV and stepped to a depolarizing potential of + 40 mV (V_c) using a pulse duration (P_d) of 250 ms. Cells were stimulated with an interpulse interval of 45 s to prevent cumulative inactivation, a property of Kv1.3 channels (Cook & Fadool, 2002; Kupper *et al*., 1995; Marom & Levitan, 1994). HisMgTx, QDs, or QDMgTx were applied directly to the bath to measure change in Kv1.3 current properties in response to peptide inhibitor, nanoparticle, or conjugate.

2.6.3 | Nano-labeling of Kv1.3 channel in HEK293 cells

HEK293 cells were grown on 12-mm glass coverslips (Cat. #12-545-90; Thermo-Fisher Scientific) and were transfected with Kv1.3 or pcDNA3 cDNA at 70%–80% confluency. At 48 hr post-transfection, cells were washed twice with HEK293 bath solution to ensure that channels were in an open state so that QDMgTx could bind the open pore of the channel. Cells were then incubated with the QDMgTx conjugate in PBS (1:15; 50 nM QD, 750 nm HisMgTx) for 30 min, permeabilized with 0.2% Triton X-100 in PBS (Cat. #9002-93-1; Thermo Fisher Scientific) for 10 min, fixed with freshly prepared 4% paraformaldehyde in PBS (Thermo-Fisher Scientific, Cat. #BP531-25) for 10 min, and then nuclear stained with 4′,6-diamidino-2-phenylindole (DAPI, Cat. #D1306; Thermo-Fisher Scientific). All incubations were performed at RT. Cells were rinsed with PBS twice between each step. Coverslips were mounted to glass slides for imaging using Fluoromount-G mounting media (Cat. #0100-01; Southern Biotech). Slides were viewed by light and fluorescent microscopy (Axioert S100; Zeiss) and signals were detected from the emissions of DAPI (340–380 nm excitation/435–485 nm emission) and QDs (532–587 nm excitation/608–683 nm emission). Individual digital images were acquired using a Zeiss Axiocam digital camera and AxioVision software, then were overlaid using Adobe Photoshop (Adobe Systems). Fluorescence intensity was determined using ImageJ (NIH) using a protocol described by Luke Hammond at The University of Queensland (https://theolb.readthedocs.io/en/latest/imaging/measuring-cell-fluorescence-using-imagej.html), whereby the mean gray value (fluorescent intensity) was measured across a uniform region of interest (ROI) and the corrected total cell fluorescence (CTCF) was determined as CTCF = integrated density − (ROI area × mean fluorescence of background readings). Data were averaged over a sample of five sets of transfected HEK293 cells.

2.7 | Experiment 3. QD functional effect on olfactory bulb using ex vivo slice electrophysiology

P21–P35 C57Bl/6J mice were anesthetized by inhalation of isoflurane (see Ethics section) and quickly decapitated, and then the OBs were exposed by removing the dorsal and lateral portions of the skull between the lambda suture and cribriform plate. The OBs were harvested and 300-μm coronal sections prepared using ice-cold oxygenated sucrose-modified ACSF solutions during vibratome sectioning (Vibratome/Leica Model 1000, Wetzlar, Germany), as previously described (Fadool *et al*., 2011; Thiebaud *et al*., 2016). Then slices were allowed to recover in an interface chamber containing oxygenated ACSF (Krimer & Goldman-Rakic, 1997) for 20–30 min at 33°C and then were maintained at RT for 60 min before recording. Recordings from OB slices were made at RT using a continuously perfused (Ismatec; 1 ml/min), submerged-slice recording chamber (RC-26; Warner Instruments) with ACSF. Slices were visualized at 10 × and 40 × using an Axioskop 2FS Plus microscope (Carl Zeiss Microimaging, Inc.) equipped with infrared detection capabilities (Dage MT1, CCD100). Electrodes were fabricated from borosilicate glass (Hilgenberg Cat. #1405002) to a pipette resistance of 4–7 MΩ. Following determination of spike threshold, cells were stimulated with a long, perithreshold current step (typically ranging from 5 to 50 pA) for 5,000 ms every 10 s to acquire spike frequency data under ASCF conditions (Control). After recording for a minimum of 10 min, the bath was switched to QDs in ASCF (QD) and spike firing frequency was measured using the same current injection for 10 min. Finally, the bath was switched a third time to apply QDMgTx to the slice and the spike firing frequency was again measured for a minimum of 10 min. The final working concentration of QDMgTx added to the bath for these slice experiments was 10 nM.

2.8 | Experiment 4. QDMgTx/HisMgTx effect on metabolism determined using Comprehensive Laboratory Animal Metabolic System

2.8.1 | Osmotic mini-pump surgery

Mice were weaned at P24 to MHF diet for a mean of 7.5–8 months prior to surgical placement of an osmotic mini-pump to deliver QDMgTx/HisMgTx or control treatments. We assembled cannulated

Alzet micro-osmotic mini-pumps (Cat. #1002; Durect Corporation) to allow for continuous delivery at a rate of 0.25 μl per hour over a 14-day period. The mini-pumps were filled with control PBS (2% BSA), 375 nM HisMgTx, 25 nM QD, or 25 nM QDMgTx 1:15 diluted PBS (2% BSA), and were prepared as per manufacturer's protocols the evening prior to surgeries. Animals were anesthetized with a continuous flow of isofluorane and were given 0.1 mg/kg buprenorphine HCl (Cat. #NDC42023-179-01; PAR Pharmaceuticals) for pain management. Mice were restrained in a Stoelting/Kopf Instruments stereotaxic apparatus and two holes were drilled (Stoelting, micromotor high-speed drill model 51,449) into the skull of the animal above the OB at the mitral cell layer coordinates (AP −0.25 mm from bregma, M/L ±0.075 and D/V −2.25 mm from dura). Cannula (Cat. #3280PD-1.5-SPC OP CONN28 gauge DBL; Plastics One) were bilaterally inserted (inter-cannula distance = 1.5 mm; cannula depth = 2.25 mm) into the holes and then a fitted Y connector (21Y connector Cat. # 37,200 81003720001F; Plastics One) delivered the pump contents to the cannula. The mini-pump itself was inserted in a pocket created under the skin on the back of the animal. The cannula were adhered to the skull using cement and the skin was closed on the back and neck using surgical staples (Clay Adams wound clips Cat. # 427,631, 9 mm; Becton Dickinson). Mice were closely monitored on a heating pad in their home cage while recovering from initial anesthesia and were administered a second dose of buprenorphine HCl under anesthesia during the first 12 hr of recovery. Mice were allowed to fully recover for 24 hr in the Comprehensive Laboratory Animal Metabolic System (CLAMS; Columbus Instruments; RRID:SCR_016718) home cages, where they were provided moistened food out of the hopper on the cage floor.

Following CLAMS assessment, mice were histologically prepared to confirm cannula placement. Briefly, mice were anesthesized with a ketamine/xylazine mix (80 mg/kg and 10 mg/kg) to reach anesthetic plane 2, and then killed via intracardial perfusion with PBS and 4% paraformaldehyde (Cat. #411678; ThermoFisher Scientific). The skulls were post-fixed in 4% paraformaldehyde/PBS overnight and decalcified for 6–9 days in 0.3 M EDTA (Cat. #5311; ThermoFisher Scientific). Extracted brains were cryoprotected in 10% then 30% sucrose/PBS at 4°C before being frozen in OCT compound-embedding medium (Cat. #4585; Fisher Healthcare). Frozen tissue was stored at −80°C until day of cryosectioning. Cryosectioning was performed on a LEICA model CM1850 cryostat (Leica Microsystems) to yield OB coronal sections at 16 μm thickness that were transferred to 1% gelatin-coated Superfrost slides (Cat. #48311, VWR International) and stored at −20°C. OB sections were stained with cresyl violet as previously described (Fadool *et al*., 2000), then viewed by light microscopy (Zeiss Axiovert, Model #S100) to confirm cannula precision.

2.8.2 | Glucose tolerance, indirect calorimetry, and metabolic assessment

The experimental workflow of the glucose tolerance testing, CLAMS metabolic assessment, and surgical implantation of osmotic mini-pumps is diagramed in Figure 6a. The strategy was to perform an intraperitoneal glucose tolerance test (IPGTT) prior and subsequent to drug delivery and allow mice to acclimate to the CLAMS chambers prior to surgery to achieve a baseline, thereby collecting pre- and post-metabolic parameters in response to the QD drug delivery within subjects. For the IPGTT, mice were fasted during the dark phase for 12 hr and then tail blood samples were acquired to monitor clearance of serum glucose over time in response to 2.5 μg/ml glucose per kg body weight (University of Virginia Vivarium Protocols, Susanna R. Keller). Glucose levels were measured using an Ascensia Contour Blood Glucose Monitoring System (Ascensia Diabetes Care US, Inc.).

Metabolic parameters, oxygen consumption (VO_2; ml/kg/min), carbon dioxide production (VCO_2; ml/kg/min), respiratory exchange ratio (RER), energy expenditure (EE; kcal/h), locomotor activity, and caloric and water intake were measured using the CLAMS system (Bell & Fadool, 2017; Fadool & Kolling, 2020). Mice had ad libitum access to food and water in overhead feeders attached to electronic balances that could detect both disturbance (meal duration) and decrease in food mass (meal size). The design of the feeder (Cat. # CLAMS—HC, Homecage) allows placement of the food in a familiar location, and in pellet form, so that there is a catch tray that accounts for weight of crumbs with minor spillage. VO_2 and VCO_2 were normalized with respect to body weight in kilograms. RER was calculated as VCO_2/VO_2. EE was calculated according to the Lusk Equation $(3.815 + 1.232 \times \text{RER}) \times VO_2$ (Lusk, 1924). Further information concerning the calculation of these metabolic variables by the CLAMS can be found online as a helpful resource (https://www.slideshare.net/InsideScientific/measuring-energy-balance-in-mice-from-vo2vco2-food-intake-and-activity-data). Locomotor activity was continuously recorded using optical beams along the x-axis of the cage so that consecutive photo-beam breaks could be scored as ambulatory movement. All data were recorded in intervals using Oxymax software (CLAX; Columbus Instruments) and each interval measurement represented the average value during a 30 s sampling period per cage. In total, mice were housed in the CLAMS for 19 days (−4 to + 14; see Figure 6a). No data were acquired in the CLAMS during the first 2 days in the chambers (−4 to −2) to permit acclimation to the environment or during the 24 hr recovery from surgery (0 to 1). The 48 hr after acclimation was used for baseline determination (−2 to 0) and this average was used to normalize data acquired for individual mice for the 11 days subsequent to drug delivery (1 to 11). Data are graphed in a normalized fashion in order to visually compare the response of drug treatment across mouse subjects for a particular metabolic variable, and non-normalized data were used in a paired-subject analysis (repeated measure) as described in the statistical analyses below.

2.9 | Data and statistical analyses

Statistical analyses were performed using Prism 8 software (Graph Pad). This software tests for normality using the D'Agostino-Pearson

normality test (omnibus K2). Significantly different means were calculated at the 95% confidence level or $\alpha \leq 0.05$, unless otherwise specified. Sample sizes of our studies were determined by A Priori Type Power Analysis applied for ANOVA and *t* test, and tested for a range of estimated means and *SD* for biophysical and metabolic parameters that were adequate for a power of 0.80, $\alpha \leq 0.05$, G*Power Cohen *ranges* $f \leq 0.68–0.81$.

2.9.1 | Experiment 2a

In order to quantify the fluorescent intensity of QDMgTx binding to Kv1.3-transfected HEK293 cells, images at 40× magnification were analyzed and averaged across a total of five different transfection rounds. A *F*-max test for homogeneity of variance was performed and then a Student's *t* test was applied to determine if there were significantly different means in the fluorescent intensity of mock-transfected cells ($pcDNA_3$ alone) versus that of Kv1.3-transfected cells.

2.9.2 | Experiment 2b

Electrophysiological records were analyzed using Clampex v10.6 software (Molecular Devices/Axon Instruments), Origin v8.0 (Microcal; Borland International), and Excel v2013 (Microsoft Office). HEK293 cells were allowed to stabilize for 3–5 sweeps after achieving the whole-cell configuration. Following stabilization (taken as Time 0), peak current amplitude was measured (I_i, initial current), and then normalized as I_n/I_i (I_n, current at time n) in order to compare change in peak current amplitude prior and subsequent to peptide inhibitor or QD conjugate channel interaction. For generation of the concentration–response curves, the I_5/I_i was used to measure the drop in current amplitude for concentrations from 10^1 to 10^4 pM from a mean of 4–6 recordings at each tested concentration. In order to observe change in peak current amplitude and time course of inhibition, Kv1.3 peak current amplitude was measured prior to and following application of HisMgTx, QD, or QDMgTx. Changes in peak current amplitude (I_5/I_i) in the presence of the peptide inhibitor, nanoparticle, or conjugate at the fifth time point (T5), 225s, compared with that at the start of the recording (T0) were statistically analyzed using non-normalized data in a two-way mixed-design analysis of variance (ANOVA) using time and treatment as factors, with a Bonferroni's *post hoc* test. The sample size (N) noted in the figure legend represents number of cells recorded that were sampled across a minimum of three transfection batches. In mitral cells, changes in action potential firing frequency were tested for statistical significance using a repeated measure, one-way ANOVA, and Bonferroni's *post hoc* test. The sample size (N) noted in the figure legend represents the number of cells that were recorded across three mice. Changes in metabolic variables (VO_2, RER, IPGTT, and bodyweight) were compared using non-normalized data in a two-way, mixed design, repeated-measures ANOVA using time and treatment as factors, followed by a Dunnett's *post hoc* test. Differences in iAUC were statistically analyzed using an ordinary one-way ANOVA with a Dunnett's *post hoc* test. All reported values are mean ± standard error of the mean (*SEM*) with indicated sample size (N) being the number of mice.

3 | RESULTS

3.1 | QD synthesis and conjugation to MgTx

3.1.1 | Production of recombinant HisMgTx

MgTx was previously produced via recombinant expression in the bacterium *E. coli* and the yeast *Pichia pastoris* (Anangi *et al*., 2012; Garcia-Calvo *et al*., 1993). We explored production via *P. pastoris* and chemical synthesis, and constructs prepared using these methods were used for preliminary experiments. However, recombinant expression in *E. coli* proved to be the most efficient method for our purposes. Here, recombinant HisMgTx was produced using a pET-28b vector transformed into BL21 SHuffle T7 Express *E. coli*. The pET-28b vector enabled expression of MgTx with an N-terminal His_6 tag, which was used for affinity purification and QD binding. An acrylamide gel summarizing the expression and affinity purification is shown in Figure 1a, and the affinity-purified product was purified to homogeneity using C18 RP-HPLC (Figure 1b). The mass of HisMgTx estimated from the gel is higher than expected (~9 kDa), likely because of its high isoelectric point (pI 9.46) reducing its electrophoretic mobility. The mass of the peptide determined using LC-MS/MS (Figure 1c) was found to be equivalent to the predicted mass (experimental = 6,475.85 Da, predicted = 6,473.53 Da).

3.1.2 | Metal-histidine–mediated self-assembly of QDMgTx

Metal-histidine–mediated self-assembly of QDMgTx allowed control over the orientation as well as the valence of peptide per QD. The addition of a terminal His_6 tag is commonly used during protein expression in bacteria or during protein synthesis, thus, can be easily applied to conjugate these biomolecules to QDs via polyimadazole-to-metal coordination (Dennis *et al*., 2010; Zhan *et al*., 2013). Here, we used QDs capped with a His-PIMA-ZW ligand, a compact capping ligand that allowed HisMgTx to directly access the QD surface (Figure 2a) as previously noted (Wang *et al*., 2015). The conjugation was characterized using gel electrophoresis in which greater amounts of QD bound to HisMgTx were identified as increased mass (Figure 2b). A decrease in mobility of QDs was observed with an increase in the amount of HisMgTx-conjugated per QD. Negligible migration of conjugates was observed as the molar ratio of QD:HisMgTx was increased to and above 1:30, suggesting that the QD surface was saturated with peptide. In Figure 2c,d, the gel was stained with Coomassie blue to identify any unbound peptide

following the conjugation. A lane containing HisMgTx alone or BSA alone (carrier protein for HisMgTx) served as controls. No HisMgTx bands were observed in the 1:5, 1:10, or 1:15 conjugates, indicating that all peptide used for the conjugation was bound to the QDs. HisMgTx bands were observed in the 1:20 and 1:25 conjugations, indicating that following conjugation in these conditions, there was excess peptide not bound to the surface of the QDs. This is in agreement with previous studies in which metal-histidine–mediated self-assembly was similarly used (Medintz *et al*., 2004). Because the 1:15 QDMgTx conjugate had the largest amount of bound HisMgTx with no observable unbound peptide, our electrophysiological and metabolic analyses used this version of the conjugate.

3.2 | Testing QD targeting and function using heterologously expressed Kv1.3 channels

3.2.1 | QDMgTx can label HEK293 cells expressing Kv1.3

Kv1.3- or $pcDNA_3$-transfected HEK293 cells were incubated with bath-applied QDMgTx to determine labeling of the conjugate in Kv1.3-transfected cells. QDMgTx labeling was strongly observed in Kv1.3-transfected cells (Figure 3a) and less so under $pcDNA_3$ transfection conditions (Figure 3c). The conjugate appeared to non-specifically bind to $pcDNA_3$-transfected cells with a significantly lower fluorescence intensity than that of Kv1.3-transfected cells (Figure 3d; 79.7 ± 10.4 for $pcDNA_3$ versus. 129.0 ± 18.0 for Kv1.3, $n = 5$, Student's t test, * $p = .0227$). When Kv1.3-transfected cells were incubated with QDs alone (Figure 3b), no measurable labeling was observed.

3.2.2 | Inhibition of Kv1.3 by HisMgTx and QDMgTx

MgTx is reported to block Kv1.3 with an IC_{50} of 11.7–119 pM (Garcia-Calvo *et al*., 1993; Knaus *et al*., 1995), and therefore we measured the ability of HisMgTx and QDMgTx to block Kv1.3 in HEK293 cells (Figure 4). Addition of the epitope tag lowered the affinity of the peptide inhibitor, but HisMgTx still blocked Kv1.3 with picomolar affinity (IC_{50} = 487 ± 106 pM, Hill coefficient = 1). Compared to HisMgTx, the 1:15 QDMgTx blocked Kv1.3 at a lower, but still picomolar affinity (IC_{50} = 825 ± 260 pM, Hill

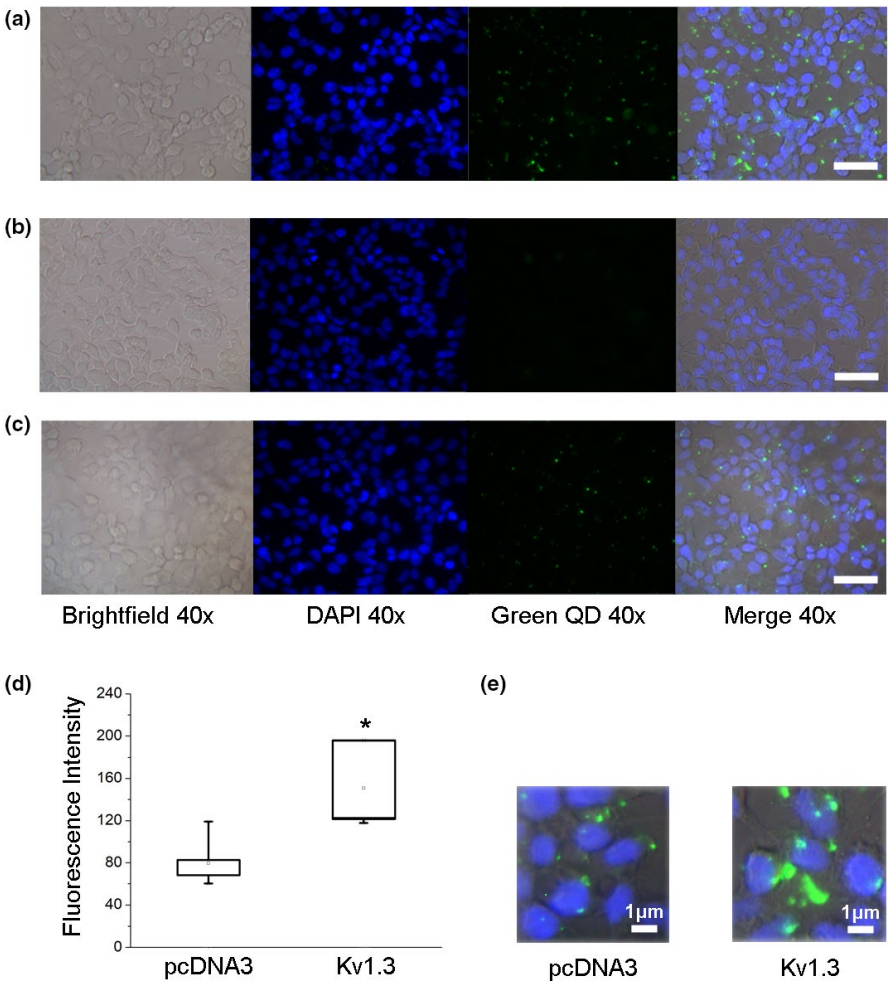

FIGURE 3 Quantum dot margatoxin conjugate (QDMgTx) can label HEK293 cells expressing Kv1.3. Photomicrographs of HEK293 cells transfected with Kv1.3 and incubated with (a) 50 nM QDMgTx 1:15 or (b) 50 nM QDs. (c) Photomicrographs of HEK293 cells transfected with $pcDNA_3$ and incubated with 50 nM QDMgTx, scale bar = 10 μm. (d) Box plot and (e) enlarged photomicrographs to quantify/visualize fluorescence intensity of the labeling in experiments (a) and (c), respectively. Box determined by the 25th and 75th percentiles and whiskers indicate 5th and 95th percentiles; $n = 5$ transfection batches for each condition. Student's t test, *Significantly different, $p = .0227$

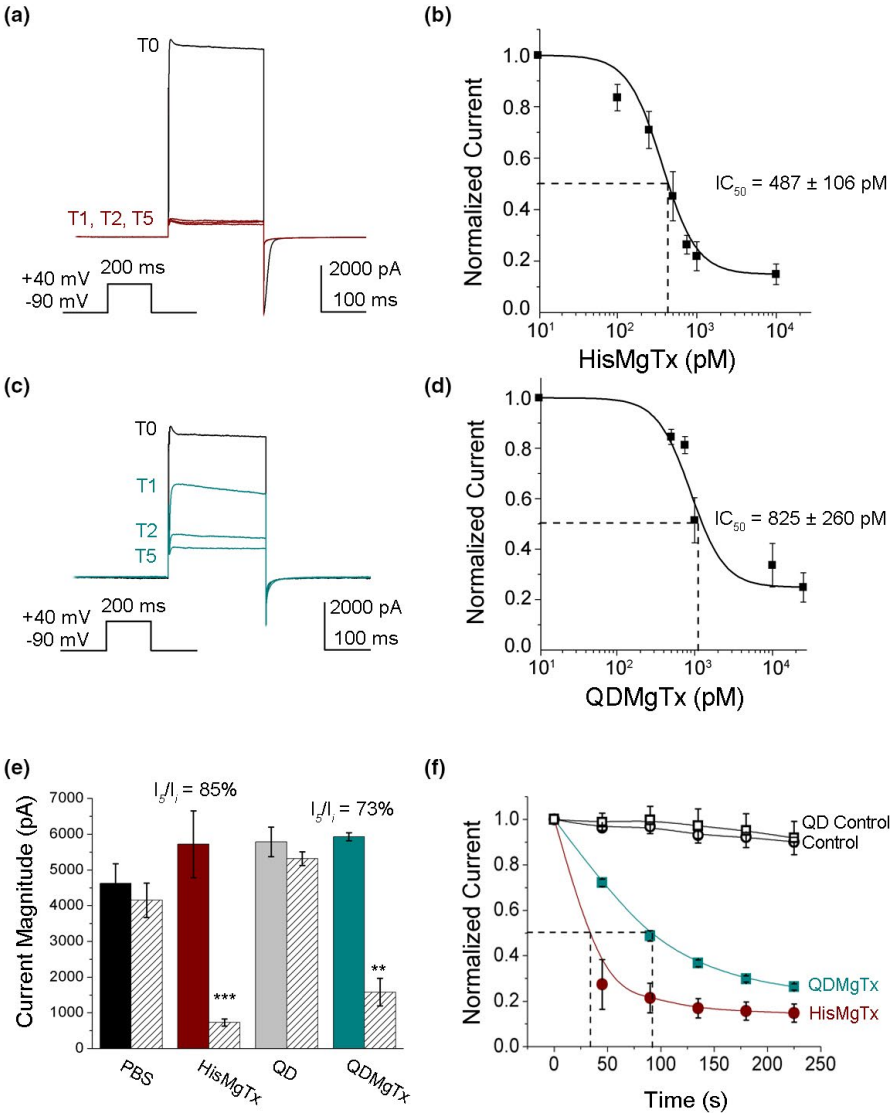

FIGURE 4 Inhibition of Kv1.3 currents by HisMgTx and its QD conjugate. Representative whole-cell patch recording of a HEK293 cell transfected with Kv1.3 (Time 0; T0) and monitored for block of voltage-activated currents following bath application of (a) HisMgTx or (c) QDMgTx. Inhibitors were bath applied using a 10 nM concentration. V_h = −90 mV, V_c = +40 mV, IPI = 45 s. (b, d) Concentration–response curves for inhibition of Kv1.3 under conditions (a) and (c), respectively; HisMgTx, IC_{50} = 487 ± 106 pM. n = 5 for each concentration tested. QDMgTx, IC_{50} = 825 ± 260 pM, n = 4–6 for all concentrations tested. (e) Peak current amplitude at time 0 (T_0) versus. time 5 (T_5) for a population of recordings, where HisMgTx, unconjugated QDs, or QDMgTx was applied to the bath solution. Values represent mean ± *SEM*, n = 16 for phosphate-buffered saline (PBS) control, and n = 4–5 for all other conditions. Two-way mixed-design analysis of variance (ANOVA) using time as a factor; Bonferroni's *post hoc* test. ***$p < .001$; **$p < .01$. (f) Normalized peak current amplitude (I_i = current initial; I_n = current at n time point) versus time for the population of recordings represented in panel e. Open circle (black) = control, closed circle (red) = HisMgTx, open square (black) = QD Control, closed square (green) = QDHisMgTx. Dotted line = time to half-maximum inhibition. Sample size (n) = number of cell recordings. HisMgTx, histidine epitope-tagged margatoxin; QDMgTx, quantum dot margatoxin conjugate

coefficient = 1; Figure 4b,d). When applied at equal concentrations (10 nM), HisMgTx and QDMgTx each significantly decreased Kv1.3 peak current amplitude (Figure 4e; two-way mixed-design analysis of variance (ANOVA) using time as a factor, $F(1,50) = 20.61$, $p < .0001$, and using treatment as a factor, $F(3,50) = 3.26$, $p = .0290$). Application of QD alone or control bath solution did not elicit a decrease in voltage-activated current over time (I_5/I_i; Figure 4e). The mean percent inhibition (at I_5/I_i) by HisMgTx versus QDMgTx was not significantly different (85 ± 3.9% for HisMgTx, n = 5 versus 73 ± 7.4% for QDMgTx, n = 4, ArcSin Transformation Student's t test, $p > .05$; Figure 4e). We measured the time required to achieve 50% inhibition of voltage-activated currents in the whole-cell patch configuration to be less than 2 min for 10 nM HisMgTx or QDHisMgTx, and the times were not significantly different (Figure 4f, 32.7 ± 10.9 s for HisMgTx, n = 5 versus. 73.4 ± 17.7 s QDMgTx, n = 4, Student's t test, $p > .05$).

3.3 | QD functional effect on OB using ex vivo slice electrophysiology

3.3.1 | QDMgTx enhances mitral cell action potential (AP) firing in olfactory bulb slices

The major output neuron of the OB is the mitral cell, with Kv1.3 making up 60%–80% of outward currents in these projection cells (Fadool & Levitan, 1998). When applied via bath application, QDMgTx significantly increased the AP firing frequency over that of control ACSF or QDs (Figure 5; one-way repeated measure (RM) ANOVA, $F(2,15) = 8.88$, $^{**}p = 0.0029$). Spike analysis demonstrated that QDMgTx and QDs decreased the pause duration between AP trains (Control, 2,511.0 ± 899.5 ms, $n = 46$; QD, 1,270.0 ± 477.9 ms, $n = 97$; QDMgTx; 1,069.0 ± 93.7 ms, $n = 43$; one-way RM ANOVA, $F(2,183) = 6.304$, $p = .0167$), while QDMgTx but not QD increased the interspike interval (ISI) within the AP train (Control, 57.4 ± 4.7 ms, $n = 73$; QD, 59.6.0 ± 8.1 ms, $n = 116$; QDMgTx; 68.0 ± 12.4 ms, $n = 61$; one-way RM ANOVA, $F(2,247) = 6.304$, $p = <.0001$). Spike analysis was acquired over a subset of 2–4 bursting cells (Control, $n = 4$; QD, $n = 3$; QDMgTx, $n = 2$). Previous reports show that MgTx (Mast & Fadool, 2012; Thiebaud *et al*., 2016) and other neuromodulators (Fadool *et al*., 2011) that act to decrease Kv1.3 activity increase the spike firing frequency and reduce the pause duration between AP trains, but have less effect on ISI.

3.3.2 | QDMgTx/HisMgTx delivery to the OB in obese mice via cannula-guided osmotic mini-pumps

Owing to our ability to inhibit Kv1.3 currents using QDMgTx in a heterologous system or in native neurons in ex vivo OB slices, we next wanted to test in vivo delivery of the inhibitor in mice by targeting native Kv1.3 channels in OB mitral cells. We initially attempted delivery of the QDMgTx/HisMgTx using an intranasal delivery (IND) technique (Hanson & Frey, 2008; Thorne *et al*., 2004) that we had previously used to deliver insulin to the OB in awake mice (Marks *et al*., 2009). Because we could not observe fluorescent labeling in the OB following IND, we were not able to determine if the lack of label was caused by failed delivery across the cribiform plate or failed detection of signal beyond the resolution limit (data not shown). Therefore, we alternatively examined whether we could localize iron-oxide magnetic nanoparticles (IOMNP) that would allow us to track delivery by ex vivo magnetic resonance imaging. A concentration of 5 mg/ml of IOMNP alone was prepared in PBS and 3 x 10 µl naris deliveries were made three times with a 2 min periodicity for a total volume of 90 µl per mouse (Marks *et al*., 2009). Images, as shown in Figure S1, were acquired using a widebore 11.75-T equipped with a Bruker Avance console and Micro2.5 imaging gradients (Bruker Biospin) at the FAMU-FSU College of Engineering (Fu *et al*., 2005; Rosenberg *et al*., 2013) using a 3D gradient-recalled echo sequence at an isotropic resolution of 50 µm. Both coronal and sagittal views of the combined OB and epithelium revealed that the IOMNP were not able to penetrate the axonal spaces in the cribiform plate to gain access to the OB neurolamina. We tried altering the time of animal sacrifice following IND, varying the concentration of IOMNP, and including known permeabilizing agents (Triton X100, hyalronidase, and chitosan), but even these variations failed to provide visualization of the magnetic nanoparticles beyond the nasal cavity, epithelium, or periphery of the brain (Figure S2).

Instead of using the IND technique, we used stereotaxically guided placement of osmotic mini-pumps to assure successful and targeted delivery of QDMgTx/HisMgTx and controls to the OB. The experimental work for the glucose tolerance testing, CLAMS metabolic assessment, and surgical implantation of osmotic mini-pumps is diagramed in Figure 6a as previously described in the methods. Each obese mouse was studied for 22 days (−7 to +14) with surgical placement of the pump after 7 days (0) (Figure 6b). Histological examination of the brains following metabolic testing was performed (Figure 6c) to confirm proper placement of the cannula using cresyl violet staining. One mouse was excluded from the data set as a result of a mistargeted cannula. In a separate cohort of non-obese mice ($n = 3$) for which cannula were clearly perforating the OB, no fluorescent QD labeling could be observed in the OB or anywhere in the brain, despite the empty osmotic capsule (Figure 6d). This result suggested that the drug treatments were osmotically delivered, but were beyond the resolution of detection of the fluorescent label.

3.4 | Assessment of QDMgTx/HisMgTx effect on metabolism using CLAMS

3.4.1 | Delivery of a Kv1.3 inhibitor to the OB of obese mice leads to a reduction in body weight and enhanced glucose clearance

Body weight and glucose clearance were monitored in obese mice receiving PBS (control), HisMgTx, or QDMgTx via cannulated delivery to the OB. HisMgTx- and QDMgTx-treated mice had a significantly reduced body weight compared to PBS control mice (Figure 7a; paired t test, $p < .05$). We compared the normalized change in body weight over time (+2 to +12) following implantation of the cannulated osmotic mini-pump (at 0; Figure 7b; two-way RM ANOVA, using time as the factor: $F(10,190) = 8.367$, $^{****}p < .0001$). There was a significant interaction of time x treatment: $F(20, 190) = 1.923$, $^{*}p < .05$. An IPGTT was performed twice on each mouse (−6, +13) to monitor their fasted ability to clear glucose prior to (Figure 7c) and after drug delivery (Figure 7d). Prior to drug treatment (−6), all mice cleared glucose similarly (two-way RM ANOVA, $p > .05$). Following drug treatment (+13), mice receiving HisMgTx or QDMgTx cleared glucose significantly faster than control animals (Figure 7d; two-way RM ANOVA using treatment: $F(2, 19) = 5.318$, $^{*}p = .0146$ and time: $F(6,114) = 53.47$, $^{***}p < .0001$ as factors). The integrated area under the curve (iAUC) is an additional measure of an animals' ability to clear glucose, and therefore we also examined how iAUC changed following drug delivery. Comparison of the iAUC

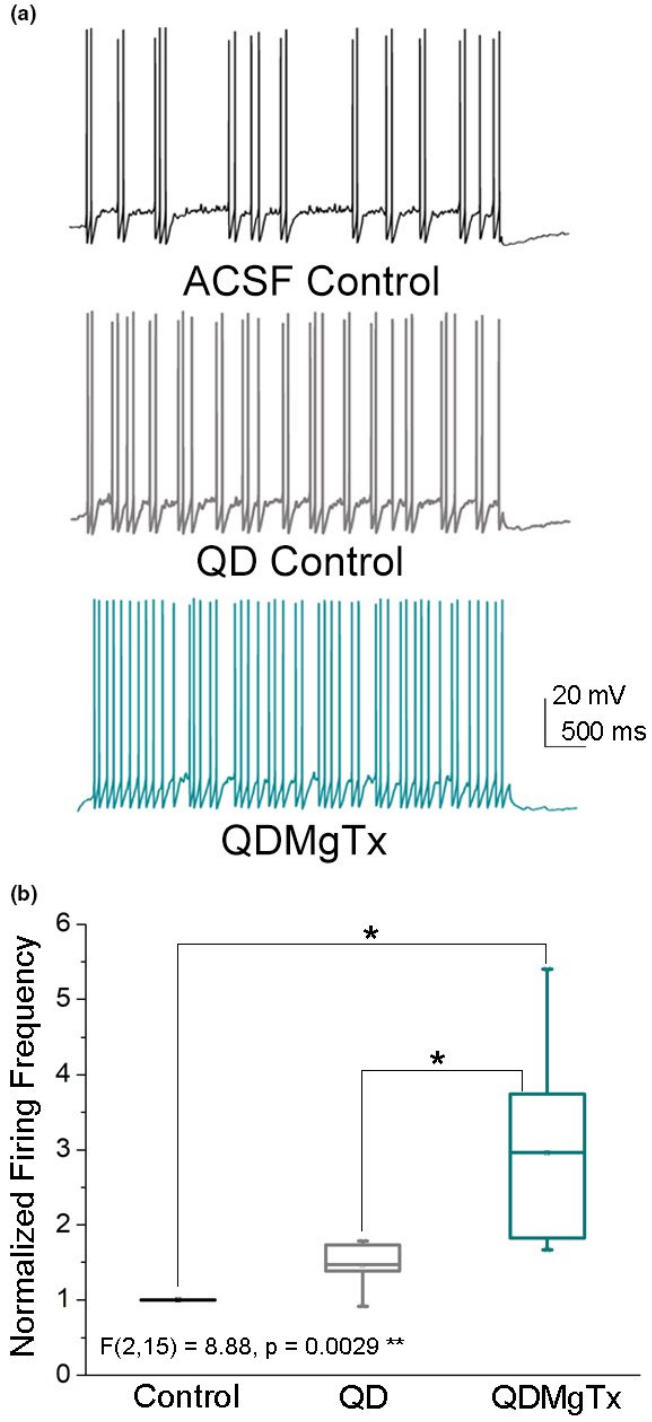

FIGURE 5 Mitral cell AP firing frequency is enhanced following application of QDMgTx. (a) Representative APs recorded in a cell sequentially introduced to bath application of artificial cerebral spinal fluid (ACSF), QD, and then QDMgTx. (b) Box plot of the normalized firing frequency for a population of MCs. One-way repeated measures ANOVA, $^{**}p < .05$; Bonferonni's *post hoc* test, Control versus QD $p > .05$; QD versus QDMgTx $^{*}p < .05$; Control versus QDMgTx $^{*}p < .05$; Box plot and whiskers notation as in Figure 3. Sample size (n) = number of cell recordings = 5

before (−6) and following (+13) drug delivery is shown in Figure 7e as a normalized change (IPGTT AUC delta). Mice receiving HisMgTx or QDMgTx had a significant change in iAUC (Figure 7e; two-way RM ANOVA using time as the factor: $F(1,19) = 19.84$, $^{***}p = .0003$), whereas control animals had no change in iAUC $p > .05$).

3.4.2 | Inhibition of Kv1.3 in the OB of obese mice does not alter the EE but reduces RER

Energy expenditure (EE), or the amount of calories burned per hour, is a compilation of resting metabolic rate, the thermic effect of eating, and energy expended during voluntary and involuntary physical movement. Following delivery of HisMgTx or QDMgTx (+2 to +12), there was no change in EE in either the light or dark cycle (Figure 8a,b; two-way RM ANOVA using treatment as the factor: light cycle: $F(2, 15) = 0.7349$, $p = .496$; dark cycle, $F(2, 15) = 1.484$, $p = .2581$). It is well known that EE can be transiently increased because of the trauma or inflammation resulting from surgery (Clark, 1973) and we observed this increase in the light cycle following surgery on Day 0 (not shown; 0.20- to 0.28-fold increase) and a subsequent lowering of EE over time ($F(9, 135) = 2.60$, $^{*}p = .0085$) for all treatments without a significance in the Bonferroni's post hoc test ($p > .05$). VO_2 is also a primary measure of metabolism. We observed no difference in VO_2 with respect to delivery of HisMgTx or QDMgTx (+2 to +12), in either the light or dark cycle (Figure 8c,d; two-way RM ANOVA using treatment as the factor: light cycle: $F(2, 15) = 0.0081$, $p = .9919$; dark cycle, $F(2, 15) = 0.2790$, $p = .7604$). We did observe an elevation in VO_2 over time that in the dark cycle that was independent of treatment (two-way RM ANOVA using time as the factor: $F(9, 135) = 2.833$, $^{**}p = .0044$). Likewise, there was no difference in carbon dioxide production (VCO_2) with respect to any treatment (Figure S3; two-way RM ANOVA using treatment as the factor: light cycle: $F(2, 15) = 0.4245$, $p = .6617$ dark cycle, $F(2, 15) = 1.035$, $p = .3793$). Interestingly, we observed a treatment effect with a measured reduction in the respiratory exchange ratio (RER) that was restricted to the light cycle (Figure 8e–f). RER is the ratio of the volume of CO_2 produced to the volume of O_2 consumed (VCO_2/VO_2) and is as indicator of which nutrients are being metabolized for energy. RER is 0.7 when lipids are being metabolized, 0.8 for proteins, and 1.0 for carbohydrates (Ramos-Jimenez *et al*., 2008). When comparing changes in RER during the light cycle (+2 to +12), there was a significant reduction in RER for animals receiving HisMgTx compared to PBS (Figure 8e, two-way RM ANOVA using with treatment as the factor: $F(2,14) = 4.677$, $^{*}p = .0278$). There was not a significant effect for QDMgTx or a time × treatment interaction, $p = .0893$. Figure 8g illustrates the mean RER for all mice (+6 to +7) to incorporate a visualization of the specific RER effect associated with the light cycle.

3.4.3 | Inhibition of Kv1.3 in the OB of obese mice may change ingestive behavior without differentially affecting locomotor activity

To complement measurements of EE, VO_2, and RER, we measured changes in total calories consumed by mice or changes in their

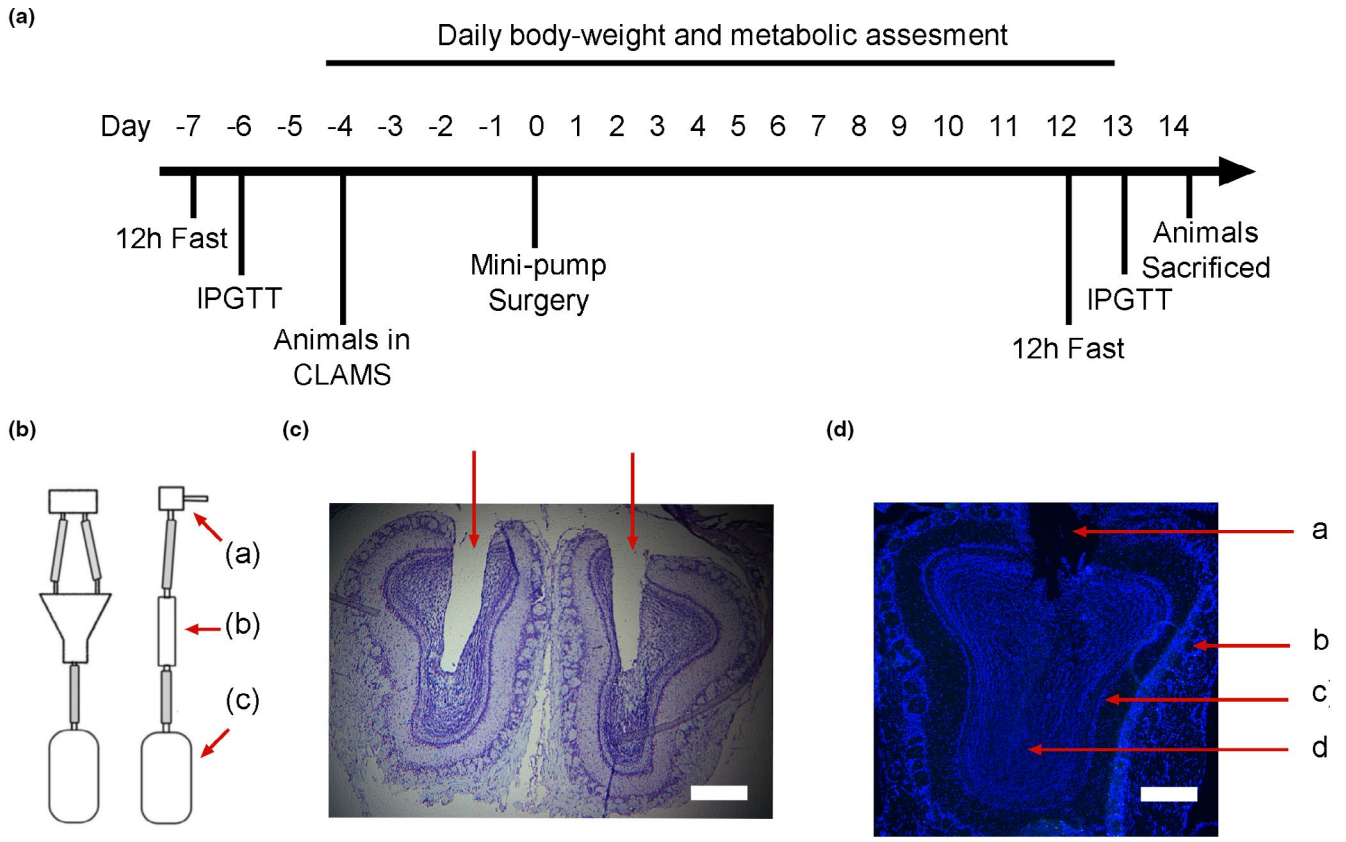

FIGURE 6 Cannula-guided osmotic mini-pump delivery of quantum dot margatoxin conjugate (QDMgTx) to the olfactory bulb (OB). (A) Schematic of experimental timeline. CLAMS, comprehensive laboratory animal metabolic system; IPGTT, intraperitoneal glucose tolerance test. (B) An Alzet osmotic mini-pump (c) was connected to bifurcated (b) cannula (a) and implanted into the OB of C57J/B6 obese mice using stereotactic guidance. (C) Photomicrograph of a pair of OBs confirming placement of the bifurcated cannula; bright field, cresyl violet stain. (D) Photomicrograph of an OB following incubation with 25 nM QDMgTx; 4′,6-diamidino-2-phenylindole stained, (a) = cannula placement, (b) = glomerular cell layer, (c) = mitral cell layer, (d) = granule cell layer; (c) and (d) scale bar = 5 μm

locomotor activity by comparing baseline values prior to and after drug delivery (−1 versus. +11, Table 1). The total caloric intake and water consumption were not significantly different for mice in any drug treatment group (paired *t* test, $p > .05$). Despite eating the same amount of calories, mice that received either HisMgTx or QDMgTx reduced their number of feeding bouts while either increasing bout duration or increasing amount of food/bout (paired *t* test, $p < .05$), neither of which were observed in the PBS control mice. HisMgTx-treated mice decreased their number of feed bouts roughly 50% while increasing the feeding duration approximately 66%. QDMgTx-treated mice also decreased their number of feed bouts roughly 50%, but had no change in feeding duration while increasing food/bout by about 30%. All mice exhibited greater ambulatory locomotor activity in the dark cycle over that of the light cycle, as anticipated for a nocturnal animal. Although individual mice varied in their baseline ambulatory activity in the dark cycle (−1), all mice exhibited significantly reduced activity regardless of drug treatment, inferring less overall locomotor activity attributed to surgery or acclimation to the CLAMS extended environment (−1 versus. 11; Table 1, paired *t*-test, $^{*}p < .05$, $^{**}p < .01$).

4 | DISCUSSION

Herein, we produced a polyhistidine-modified peptide that inhibits Kv1.3 and can be self-assembled to fluorescent QDs through a one-step metal-histidine coordination. We demonstrated that this coupling strategy did not significantly alter the inhibitor interaction with the channel as determined by electrophysiological analyses, and it allowed sufficient conjugation to permit in vivo investigation of targeted delivery to a brain area that highly expresses Kv1.3. Most significantly, we discovered that osmotic pump administered HisMgTx and QDMgTx to the OB caused a loss of body weight in DIO mice and increased their ability to clear a glucose challenge. The loss in body weight was not attributed to a change in oxygen consumption or total energy expenditure. Treatment with the peptide inhibitor alone (HisMgTx) caused a reduction in RER in the light cycle, suggesting a shift in fuel utilization to fats over that of carbohydrates by blocking Kv1.3 conductance selectively in the OB. Interestingly, this did not cause a change in total caloric consumption, rather a change in ingestive behavior whereby mice significantly decreased feeding bouts while eating longer or larger meals.

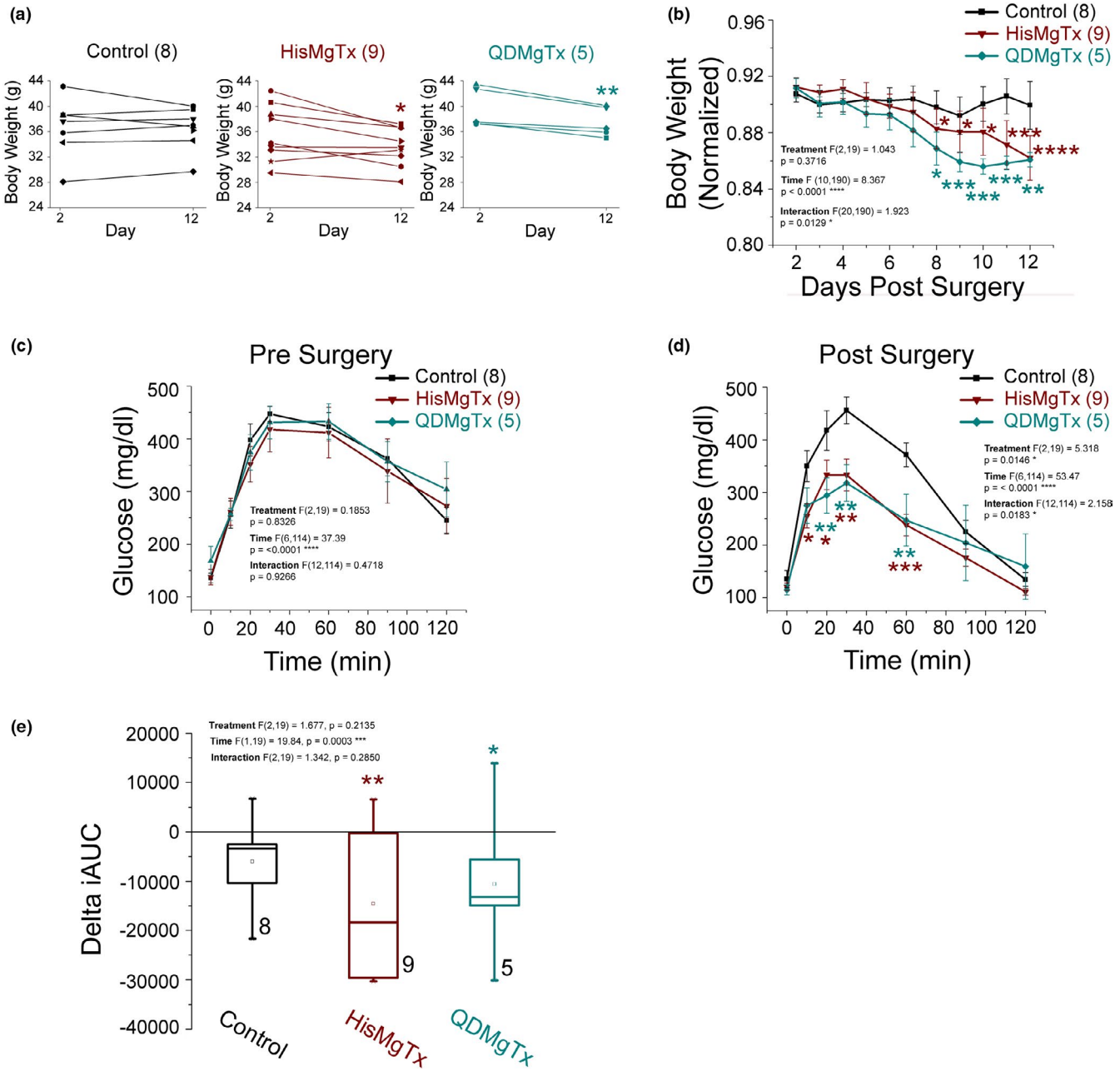

FIGURE 7 Obese mice receiving a Kv1.3 inhibitor delivered to the olfactory bulb had reduced body weight and cleared glucose more quickly. (a) Body weight on day 2 versus day 12 for individual mice. (b) Normalized body weight versus time. Glucose clearance on (c) Pre-(−6) and (d) Post-Surgery (13). (e) Box plot of the change in iAUC for data in (c–d). Data represent mean ± *SEM*. Phosphate-buffered saline (PBS): $n = 8$; HisMgTxFSU: $n = 9$; QDMgTx: $n = 5$. (a) Paired *t*-test within treatment, $^{*}p < .05$. (b–e) Two-way repeated measure ANOVA with factors of treatment, time, and interaction as noted. (b) Bonferroni's *post hoc* test $^{*}p < .05$, $^{**}p < .01$, $^{***}p < .001$, $^{****}p < .0001$ significantly different from day 2. (c–d) Bonferroni's *post hoc* test $^{*}p < .05$, $^{**}p < .01$, $^{***}p < .001$ significantly different from PBS Control. (e) One-way ANOVA, Bonferroni's *post hoc* test significantly different than Day −6, $^{*}p < .05$, $^{**}p < .01$. Sample size (n) = number of mice. HisMgTx, histidine epitope-tagged margatoxin; QDMgTx, quantum dot margatoxin conjugate

Recombinant expression of the Kv1.3 inhibitor (HisMgTx) permitted conjugation to the Zn^{2+} surface of QDs using polyhistidine-mediated self-assembly, while retaining a majority of predicted biophysical properties of the channel in a blocked state. Addition of a polyhistidine tag only slightly decreased the inhibitory potency of the peptide (IC_{50} of 487 pM compared to reported IC_{50} values

FIGURE 8 Inhibition of Kv1.3 in the olfactory bulb of obese mice reduces respiratory exchange ratio (RER) without changing energy expenditure (EE) and VO_2. Normalized EE in the (a) light and (b) dark cycle, VO_2 in the (c) light and (d) dark cycle, and RER in the (e) light and (f) dark cycle. Data represent mean ± *SEM* with number of animals per treatment group as noted. Notations and statistical analyses as in Figure 7b. (g) Mean RER of all mice over time across the light and dark cycle of days 6 and 7

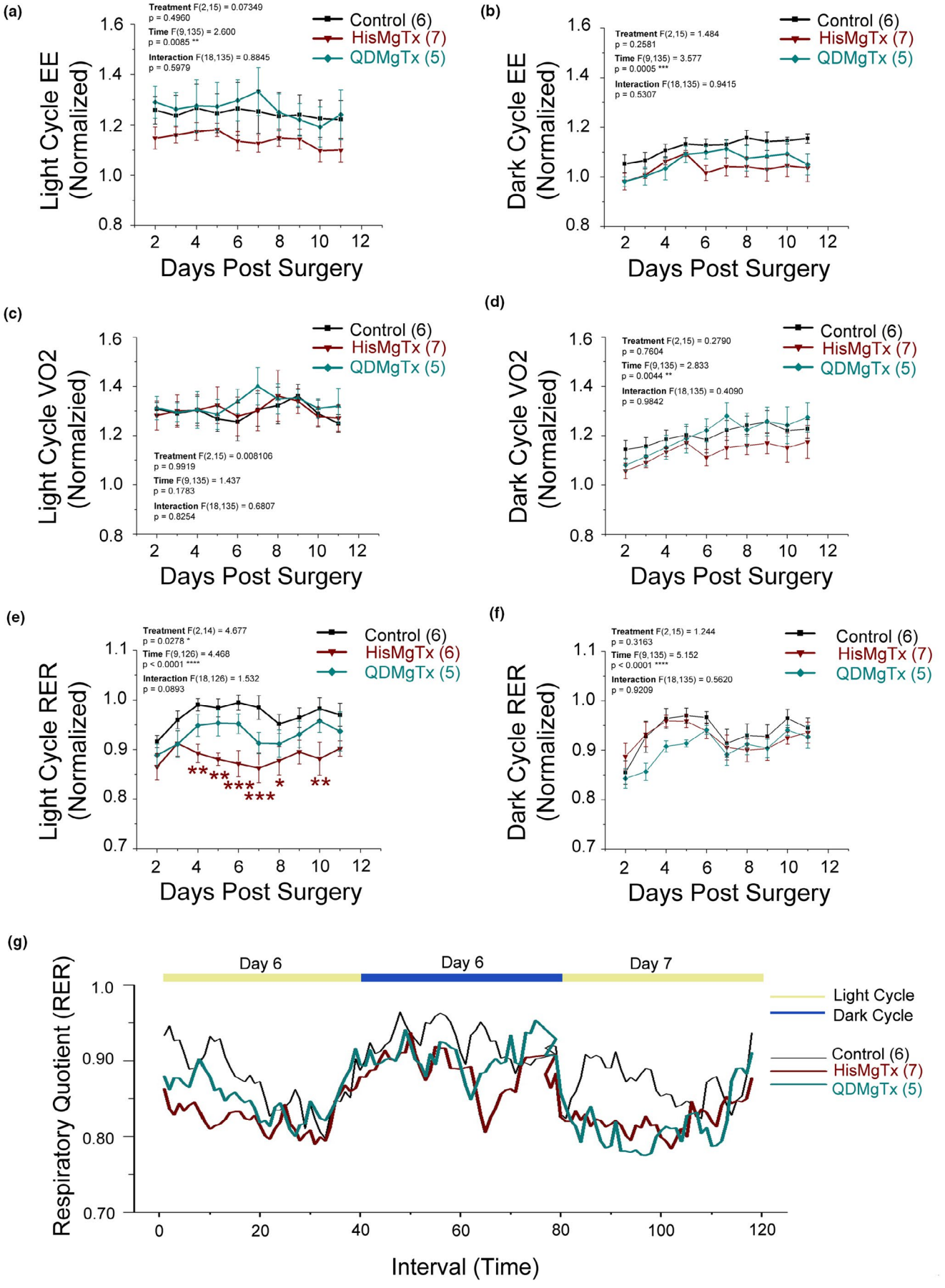
(a)
Treatment F(2,15) = 0.07349
p = 0.4960
Time F(9,135) = 2.600
p = 0.0085 **
Interaction F(18,135) = 0.8845
p = 0.5979
Control (6)
HisMgTx (7)
QDMgTx (5)
Light Cycle EE (Normalized)
Days Post Surgery
(b)
Treatment F(2,15) = 1.484
p = 0.2581
Time F(9,135) = 3.577
p = 0.0005 ***
Interaction F(18,135) = 0.9415
p = 0.5307
Dark Cycle EE (Normalized)
(c)
Treatment F(2,15) = 0.008106
p = 0.9919
Time F(9,135) = 1.437
p = 0.1783
Interaction F(18,135) = 0.6807
p = 0.8254
Light Cycle VO2 (Normalized)
(d)
Treatment F(2,15) = 0.2790
p = 0.7604
Time F(9,135) = 2.833
p = 0.0044 **
Interaction F(18,135) = 0.4090
p = 0.9842
Dark Cycle VO2 (Normalized)
(e)
Treatment F(2,14) = 4.677
p = 0.0278 *
Time F(9,126) = 4.468
p < 0.0001 ****
Interaction F(18,126) = 1.532
p = 0.0893
HisMgTx (6)
Light Cycle RER (Normalized)
(f)
Treatment F(2,15) = 1.244
p = 0.3163
Time F(9,135) = 5.152
p < 0.0001 ****
Interaction F(18,135) = 0.5620
p = 0.9209
Dark Cycle RER (Normalized)
(g)
Day 6
Day 6
Day 7
Light Cycle
Dark Cycle
Respiratory Quotient (RER)
Interval (Time)

TABLE 1 Locomotor and Feeding behavior of obese mice treated with PBS, HisMgTx, or QDMgTx via cannulated osmotic mini-pump

	PBS		HisMgTx		QDMgTx	
	Day −1	Day 11	Day −1	Day 11	Day −1	Day 11
X-Axis Beam Breaks						
12h Light (Cumulative)	4,656 ± 3,037 (6)	1552 ± 342	6,783 ± 2,403 (7)	2,667 ± 1,296	4,590 ± 2,205 (5)	1,216 ± 551
12h Dark (Cumulative)	12,495 ± 2056 (6)	6,892 ± 1627*	25,376 ± 4,464 (7)	8,649 ± 3,073**	14,935 ± 1993 (5)	5,376 ± 466*
Water Intake (g)	2.6 ± 0.3 (5)	3.1 ± 0.3	3.3 ± 0.3 (7)	3.8 ± 0.5	3.6 ± 0.5 (4)	3.2 ± 0.2
Caloric Intake (kcal)	13.9 ± 1.2 (6)	14.6 ± 0.3	14.7 ± 1.0 (7)	12.6 ± 1.5	16.0 ± 1.2 (5)	15.1 ± 0.9
Feeding Bouts	21.3 ± 1.9 (6)	18.5 ± 2.0	37.3 ± 4.1 (7)	20.0 ± 2.3*	44.6 ± 7.0 (5)	18.8 ± 3.2*
Grams/Feeding Bout	0.2 ± 0.01 (6)	0.2 ± 0.01	0.15 ± 0.01(7)	0.17 ± 0.02	0.17 ± 0.02 (5)	0.25 ± 0.01*
Feeding Duration (s)	177.4 ± 65.4 (6)	256.8 ± 60.4	133.6 ± 24.1 (7)	222.5 ± 42.9*	242.9 ± 60.6 (5)	320.3 ± 39.8

All values ± standard error of mean (*SEM*). Paired *t*-test, Day −1 versus Day 11.

*$p = .05$.

**$p < .01$.

of 112–119 pM for unconjugated peptide (Garcia-Calvo *et al*., 1993; Knaus *et al*., 1995)). Despite this small reduction in potency, block of the channel occurred quickly. MgTx is amenable as a peptide blocker because of the fact that it has an extremely slow k_{off} of 2 hr, and yet its k_{on} is also rather slow for a vestibule blocker (Fadool & Levitan, 1998; Knaus *et al*., 1995). Conjugation of the inhibitor to the QD (QDMgTx) reduced the potency of channel inhibition (IC_{50} = 894 pM), however, the binding kinetics were equally as strong as that of HisMgTx, taking an average of 32 and 73 s to reach half block, respectively. Regardless of the measured inhibitory potency of either form of the inhibitor, both had rapid association with the channel and were equally effective blockers, causing a loss of 73%–85% of the outward current in Kv1.3-expressing HEK293 cells. When tested on ex vivo slices of the OB, QDMgTx, but not QDs alone, increased AP firing frequency by decreasing the pause duration between spike trains. Although we observed that QDMgTx binds non-specifically to mock-transfected HEK293 cells, functionally, we found that QDs did not enhance excitability of mitral cells, which is consistent with their inability to block Kv1.3 voltage-activated conductance in HEK293 cells. These results suggest that the conjugated HisMgTx, not the QD, is acting to increase mitral cell excitability.

It is not clear why QDMgTx was effective in labeling Kv1.3-expressing HEK293 cells but could not be visualized in mitral cells given the slow k_{off} for the MgTx interaction with the channel. Given the confirmation of the accuracy of the cannula placement and the calculated volume of the OB with determined osmotic delivery rates, it is unlikely that the inhibitors traveled beyond the OB region. Moreover, dye tracking and viral infection at similar flow rates and injection volumes to the OB in our hands did not reveal labeling outside the OB. Certainly, catabolism or clearance of the QD is feasible given the duration of delivery, and would be a factor to reduce sustained visibility of the label in vivo. Previous studies have shown that QDs are cleared within hours or days, depending on route of delivery (Fischer *et al*., 2006; Medintz *et al*., 2008). Likewise, a greater concentration of the conjugate may also be required for in vivo delivery to visualize QDs with fluorescence microscopy, while transmission electron or confocal microscopy, as others have used (Brunetti *et al*., 2018; Dante *et al*., 2017) may be a more appropriate technique for visualizing signal at low or therapeutic concentrations.

Immobilization of polyhistidine-containing biomolecules on the Zn^{2+} surface of QDs has been widely applied and is an attractive route of conjugation (Clapp *et al*., 2004; Dif *et al*., 2009; Wang *et al*., 2016). We previously covalently conjugated MgTx to QDs by activating carboxyl groups on the designed QDs such that they would form an amide bond with basic residues found on the surface of MgTx (Schwartz *et al*., 2017). Although this method was not capable of producing sufficient yields to perform in vivo studies, it produced a conjugate that inhibited voltage-activated Kv1.3 currents (66% inhibition) in HEK293 cells and was selective to Kv1.2 and 1.3 *Shaker* family members when screened for selectivity (Kv1.1 to 1.7). Although we did not retest for selectivity with our newly synthesized HisMgTx and QDMgTx conjugate, herein, we did not expect the selectivity to be different than the native MgTx peptide because the primary surface interaction of the peptide has been identified via NMR and mutational and molecular dynamic studies to be on the peptides three β-sheets (Johnson *et al*., 1994; Khabiri *et al*., 2011; Nikouee *et al*., 2012; Yu *et al*., 2004) that we did not modify.

Having now produced therapeutic quantities of HisMgTx and QDMgTx, we were interested if pharmacological inhibition of Kv1.3 in the OB could alter metabolic function in DIO mice. Previous work has shown that pharmacological inhibition of Kv1.3 or whole-body

deletion of the channel can significantly alter metabolism in mice. In the periphery, Kv1.3 is expressed in T-lymphocytes, brown fat, and white adipose tissue, whereas in the CNS, Kv1.3 is found in the dentate gyrus of the hippocampus, mitral cells in the OB, and in pyramidal cells of the pyriform cortex (Kues & Wunder, 1992; Fadool & Levitan, 1998; Marks & Fadool, 2007; Colley *et al*., 2009; Upadhyay *et al*., 2013; Al Koborssy *et al*. 2018). Whether there are differential mechanisms to reduce body weight by inhibiting Kv1.3 peripherally versus centrally is not known. When the Kv1.3 inhibitor ShK-186 was delivered to the periphery via intraperitoneal injection every other day over a 10-week period, DIO mice had improved glucose clearance and a reduction in body weight that was attributed to an activation of brown fat that increased β-oxidation of fatty acids. Mice had enhanced VO_2 and EE without a change in total caloric consumption or locomotor activity (Upadhyay *et al*., 2013). Upadhyay *et al*. (2013) reported that a peripherally administered Kv1.3 inhibitor increased RER, selectively in the light cycle, which in turn increased brown adipose tissue metabolism that may or may not have an effect on thermogenesis in humans (Carpentier *et al*., 2018). Although it is not clear if peripherally administered Kv1.3 blockers cross the blood–brain barrier, especially at the level of the olfactory system that is known to be leaky (Palouzier-Paulignan *et al*., 2012), our data demonstrate that direct application of Kv1.3 inhibitors to the OB reduces body weight in DIO mice by oppositely changing fuel metabolism (decreasing RER), improving glucose clearance, and altering ingestive behavior, rather than modifying VO_2 or EE. Our measured decrease in RER indicates an increased lipid oxidation over that of carbohydrates, but the mechanism of how this might be activated by the OB is unresolved.

In addition to increased metabolism, Kv1.3$^{-/-}$ mice also have elevated olfactory ability, in terms of both odor discrimination and odor threshold (referred to as super-smeller mice) (Fadool *et al*., 2004; Thiebaud *et al*., 2014; Tucker *et al*., 2012; Tucker *et al*., 2008; Tucker *et al*., 2012; Xu *et al*., 2003). Kv1.3$^{-/-}$ mice have smaller, supernumerary glomeruli, increased density of odorant receptors, and can discriminate odor molecules that differ by only one carbon atom (Biju *et al*., 2008; Fadool *et al*., 2004). While super-smeller mice do not have changed caloric intake, they have irregular ingestive behaviors (increased meal frequency and decreased water bolus) and elevated locomotor activity (Fadool *et al*., 2004). Interestingly, genetic ablation of olfactory sensory neurons, resulting in a loss of olfactory ability, was shown to selectively reduce body weight in DIO but not control fed mice (Riera *et al*., 2017). The reduction in body weight occurred without a change in caloric intake but rather a significant increase in VO_2 and EE in both the light and dark cycle. The reduction in body weight was thought to be caused by an activation of white and brown fat to increase lipolysis. A recent study (Mutlu *et al*., 2020) identified select olfactory neurons in *C. elegans* that could regulate fat metabolism without altering ingestive behavior. Inhibition of neuropeptide olfactory circuits in the worm revealed a molecular mechanism using glucocorticoid-inducible kinase to regulate fat metabolism in an odor-specific fashion. This further suggests that olfactory physiology can influence metabolic function.

Nutritional status is well understood to influence olfactory physiology. In the OB, Kv1.3 is expressed in mitral cells, the primary projection neurons of the OB that project to higher regions of the brain via the lateral olfactory tract. Mitral cell activity is primarily stimulated by olfactory sensory input, however, feeding state and nutritional status play a role as well (Aime *et al*., 2014; Thiebaud *et al*., 2014). Glucagon-like peptide 1 (GLP-1), insulin, and glucose all increase the excitability of mitral cells by reducing Kv1.3 activity (Fadool & Levitan, 1998; Fadool *et al*., 2000; Tucker *et al*., 2010; Tucker et al. 2013; Thiebaud *et al*., 2016). In obesity, GLP-1 secretions are known to be reduced from sources outside of the OB (Faerch *et al*., 2015; Ranganath *et al*., 1996) and the ability to clear glucose is limited (Thiebaud *et al*., 2014). Likewise, a concurrent reduction in olfactory ability is observed (Thiebaud *et al*., 2014). At the level of the OB, the ability of insulin to increase mitral cell activity is significantly reduced (Fadool *et al*., 2011) following diet-induced obesity. An altered action of GLP-1, insulin, and glucose on Kv1.3 in obese mice, brought on by altered levels or signaling, could lead to changed excitability of the output neurons to higher olfactory cortical and hypothalamic regions to change metabolic set-point.

Herein, we delivered HisMgTx/QDMgTx to the OB in obese mice, essentially jumpstarting a pathway dampened by nutritional state, and observed a reduction in body weight and improved glucose clearance, and with HisMgTx, a significant reduction in RER. RER is an indicator of which nutrients are being metabolized for energy and a reduction suggests a shift in fuel utilization to fats rather than carbohydrates. This identifies for the first time a unique role of the OB in energy regulation. Interestingly, central infusions of GLP-1 have similar impacts on energy regulation. GLP-1R activation in the CNS has been shown to reduce RER (Hwa *et al*., 1998; Kooijman *et al*., 2015), improve glucose clearance (Kooijman *et al*., 2015; Sandoval *et al*., 2008a, 2008b) and reduce caloric intake. Here, we observed an effect on ingestive behavior owing to HisMgTx and QDMgTx delivery to the OB, however, caloric intake was difficult to monitor because of the cannulated surgery having a significant influence on this variable. Likewise, we previously identified the unique presence of GLP-1-secreting cells known as preproglucagon neurons in the OB, however, it is unclear if these cells act as a driver of energy regulation (Thiebaud *et al*., 2016, 2019). The exact mechanism by which neuromodulation of Kv1.3 influences metabolism and fuel utilization is still under exploration, but it is clear that direct inhibition of Kv1.3 in the OB has a significant effect on metabolic function.

ACKNOWLEDGMENTS

We would like to thank Ms. Abigail Thomas and Carley Huffstetler for exceptional technical assistance, mouse husbandry, and assistance with citations. We are gracious for the epitope tagging and subcloning performed by Dr. Brian Washburn in the FSU Molecular Cloning Facility and HPLC support by Margarete Seavy in the FSU Analytical Facility. A portion of this work was performed at the National High Magnetic Field Laboratory, which is supported by the National Science Foundation (NSF) grant DMR-1644779 and

State of Florida. This work was supported by research and training awards administered by the National Institute on Deafness and other Communication Disorders (NIDCD) at the National Institutes of Health (NIH): R01DC013080, T32DC000044, and F31DC014638 and National Science Foundation (NSF-CHE, Grant no. 1508501. We are appreciative of the award of an East Asia and Pacific Summer Institutes (EAPSI) Australian Fellowship from the NSF (Award no. 1613988). This work was also supported by a FSU Legacy Fellowship, a Robinson Endowment Award from Tallahassee Memorial Hospital, and by the Stanley and Shirley Marshall Endowment Fund. All constructs produced in this work (HisMgTx, QDs, and QDMgTx) can be shared upon request. G.F.K. was supported by a Principal Research Fellowship (APP1136889) from the Australian National Health & Medical Research Council.

All experiments were conducted in compliance with the ARRIVE guidelines.

CONFLICT OF INTEREST

The authors have no interests to declare, scientific or financial.

ORCID

Austin B. Schwartz https://orcid.org/0000-0002-8059-7577
Anshika Kapur https://orcid.org/0000-0002-0154-5171
Zhenbo Huang https://orcid.org/0000-0003-4857-5500
Raveendra Anangi https://orcid.org/0000-0003-2268-6288
John M. Spear https://orcid.org/0000-0002-4210-791X
Scott Stagg https://orcid.org/0000-0002-4210-791X
Erminia Fardone https://orcid.org/0000-0001-7123-9551
Zolan Dekan https://orcid.org/0000-0002-6841-4176
Jens T. Rosenberg https://orcid.org/0000-0002-2978-3104
Samuel C. Grant https://orcid.org/0000-0001-7738-168X
Glenn F. King https://orcid.org/0000-0002-2308-2200
Hedi Mattoussi https://orcid.org/0000-0002-6511-9323
Debra Ann Fadool https://orcid.org/0000-0002-0546-3720

REFERENCES

Aime, P., Palouzier-Paulignan, B., Salem, R., Al, K. D., Garcia, S., Duchamp, C., Romestaing, C., & Julliard, A. K. (2014). Modulation of olfactory sensitivity and glucose-sensing by the feeding state in obese Zucker rats. *Frontiers in Behavioral Neuroscience*, *8*, 326.

Al Koborssy, D., Palouzier-Paulignan, B., Canova, V., Thevenet, M., Fadool, D. A., & Julliard, A. K. (2018). Modulation of olfactory-driven behavior by metabolic signals: Role of the piriform cortex. *Brain Structure and Function*, *224*(1), 315–336.

Aldeek, F., Muhammed, M. A., Palui, G., Zhan, N., & Mattoussi, H. (2013). Growth of highly fluorescent polyethylene glycol- and zwitterion-functionalized gold nanoclusters. *ACS Nano*, *7*, 2509–2521. https://doi.org/10.1021/nn305856t

Aldeek, F., Safi, M., Zhan, N., Palui, G., & Mattoussi, H. (2013). Understanding the self-assembly of proteins onto gold nanoparticles and quantum dots driven by metal-histidine coordination. *ACS Nano*, *7*, 10197–10210. https://doi.org/10.1021/nn404479h

Anangi, R., Koshy, S., Huq, R., Beeton, C., Chuang, W. J., & King, G. F. (2012). Recombinant expression of margatoxin and agitoxin-2 in *Pichia pastoris*: An efficient method for production of Kv1.3 channel blockers. *PLoS One*, *7*, e52965.

Anikeeva, N., Lebedeva, T., Clapp, A. R., Goldman, E. R., Dustin, M. L., Mattoussi, H., & Sykulev, Y. (2006). Quantum dot/peptide-MHC biosensors reveal strong CD8-dependent cooperation between self and viral antigens that augment the T cell response. *Proceedings of the National Academy of Sciences of the United States of America*, *103*, 16846–16851.

Antunes, G., Sebastião, A. M., & Simoes de Souza, F. M. (2014). Mechanisms of regulation of olfactory transduction and adaptation in the olfactory cilium. *PLoS One*, *9*(8), e105531. https://doi.org/10.1371/journal.pone.0105531

Bell, G. A., & Fadool, D. A. (2017). Awake, long-term intranasal insulin treatment does not affect object memory, odor discrimination, or reversal learning in mice. *Physiology and Behavior*, *174*, 104–113. https://doi.org/10.1016/j.physbeh.2017.02.044

Biju, K. C., Marks, D. R., Mast, T. G., & Fadool, D. A. (2008). Deletion of voltage-gated channel affects glomerular refinement and odorant receptor expression in the mouse olfactory system. *The Journal of Comparative Neurology*, *506*, 161–179. https://doi.org/10.1002/cne.21540

Brunetti, J., Riolo, G., Gentile, M., Bernini, A., Paccagnini, E., Falciani, C., Lozzi, L., Scali, S., Depau, L., Pini, A., Lupetti, P., & Bracci, L. (2018). Near-infrared quantum dots labelled with a tumor selective tetrabranched peptide for in vivo imaging. *Journal of Nanobiotechnology*, *16*, 21. https://doi.org/10.1186/s12951-018-0346-1

Carpentier, A. C., Blondin, D. P., Virtanen, K. A., Richard, D., Haman, F., & Turcotte, E. E. (2018). Brown adipose tissue energy metabolism in humans. *Frontiers in Endocrinology*, *9*, 447. https://doi.org/10.3389/fendo.2018.00447

Clapp, A. R., Goldman, E. R., & Mattoussi, H. (2006). Capping of CdSe-ZnS quantum dots with DHLA and subsequent conjugation with proteins. *Nature Protocols*, *1*, 1258–1266. https://doi.org/10.1038/nprot.2006.184

Clapp, A. R., Medintz, I. L., Mauro, J. M., Fisher, B. R., Bawendi, M. G., & Mattoussi, H. (2004). Fluorescence resonance energy transfer between quantum dot donors and dye-labeled protein acceptors. *Journal of the American Chemical Society*, *126*, 301–310.

Clark, R. G. (1973). Metabolic-states in relation to surgery and anesthesia. *Proceedings of the Royal Society of Medicine*, *66*(8), 765–767. https://doi.org/10.1177/003591577306600816

Coecke, S., Balls, M., Bowe, G., Davis, J., Gstraunthaler, G., Hartung, T., Hay, R., Merten, O.-W., Price, A., Schechtman, L., Stacey, G., & Stokes, W. (2005). Guidance on good cell culture practice. A report of the second ECVAM task force on good cell culture practice. *Alternatives to Laboratory Animals*, *33*, 261–287. https://doi.org/10.1177/026119290503300313

Colley, B. S., Cavallin, M. A., Biju, K., Marks, D. R., & Fadool, D. A. (2009). Brain-derived neurotrophic factor modulation of Kv1.3 channel is disregulated by adaptor proteins Grb10 and nShc. *BMC Neuroscience*, *10*, 8. https://doi.org/10.1186/1471-2202-10-8

Colley, B., Tucker, K., & Fadool, D. A. (2004). Comparison of modulation of Kv1.3 channel by two receptor tyrosine kinases in olfactory bulb neurons of rodents. *Receptors and Channels*, *10*, 25–36. https://doi.org/10.3109/10606820490270870

Cook, K. K., & Fadool, D. A. (2002). Two adaptor proteins differentially modulate the phosphorylation and biophysics of Kv1.3 ion channel by SRC kinase. *Journal of Biological Chemistry*, *277*, 13268–13280.

Dante, S., Petrelli, A., Petrini, E. M., Marotta, R., Maccione, A., Alabastri, A., Quarta, A., De Donato, F., Ravasenga, T., Sathya, A., Cingolani, R., Proietti Zaccaria, R., Berdondini, L., Barberis, A., & Pellegrino, T. (2017). Selective targeting of neurons with inorganic nanoparticles: Revealing the crucial role of nanoparticle surface charge. *ACS Nano*, *11*, 6630–6640. https://doi.org/10.1021/acsnano.7b00397

Dennis, A. M., Sotto, D. C., Mei, B. C., Medintz, I. L., Mattoussi, H., & Bao, G. (2010). Surface ligand effects on metal-affinity coordination

to quantum dots: Implications for nanoprobe self-assembly. *Bioconjugate Chemistry*, *21*, 1160–1170.

Dif, A., Boulmedais, F., Pinot, M., Roullier, V., Baudy-Floc'h, M., Coquelle, F. M., Clarke, S., Neveu, P., Vignaux, F., Le, B. R., Dahan, M., Gueroui, Z., & Marchi-Artzner, V. (2009). Small and stable peptidic PEGylated quantum dots to target polyhistidine-tagged proteins with controlled stoichiometry. *Journal of the American Chemical Society*, *131*, 14738–14746.

Dossat, A. M., Lilly, N., Kay, K., & Williams, D. L. (2011). Glucagon-like peptide 1 receptors in nucleus accumbens affect food intake. *Journal of Neuroscience*, *31*, 14453–14457. https://doi.org/10.1523/JNEUROSCI.3262-11.2011

Fadool, D. A., & Kolling, L. J. (2020). Role of olfaction for eating behavior. In B. Fritzsch, & W. Meyerhoff (Eds.), *The senses: A comprehensive reference* (p. 43). Netherlands: Elsevier.

Fadool, D. A., & Levitan, I. B. (1998). Modulation of olfactory bulb neuron potassium current by tyrosine phosphorylation. *Journal of Neuroscience*, *18*, 6126–6137. https://doi.org/10.1523/JNEUROSCI.18-16-06126.1998

Fadool, D. A., Tucker, K., & Pedarzani, P. (2011). Mitral cells of the olfactory bulb perform metabolic sensing and are disrupted by obesity at the level of the Kv1.3 ion channel. *PLoS One*, *6*, e24921.

Fadool, D. A., Tucker, K., Perkins, R., Fasciani, G., Thompson, R. N., Parsons, A. D., Overton, J. M., Koni, P. A., Flavell, R. A., & Kaczmarek, L. K. (2004). Kv1.3 channel gene-targeted deletion produces "Super-Smeller Mice" with altered glomeruli, interacting scaffolding proteins, and biophysics. *Neuron*, *41*, 389–404. https://doi.org/10.1016/S0896-6273(03)00844-4

Fadool, D. A., Tucker, K., Phillips, J. J., & Simmen, J. A. (2000). Brain insulin receptor causes activity-dependent current suppression in the olfactory bulb through multiple phosphorylation of Kv1.3. *Journal of Neurophysiology*, *83*, 2332–2348. https://doi.org/10.1152/jn.2000.83.4.2332

Faerch, K., Torekov, S. S., Vistisen, D., Johansen, N. B., Witte, D. R., Jonsson, A., Pedersen, O., Hansen, T., Lauritzen, T., Sandbaek, A., Holst, J. J., & Jorgensen, M. E. (2015). GLP-1 response to oral glucose is reduced in prediabetes, screen-detected Type 2 diabetes, and obesity and influenced by sex: The ADDITION-PRO study. *Diabetes*, *64*, 2513–2525. https://doi.org/10.2337/db14-1751

Fischer, H. C., Liu, L., Pang, K. S., & Chan, W. C. W. (2006). Pharmacokinetics of nanoscale quantum dots: In vivo distribution, sequestration, and clearance in the rat. *Advanced Functional Materials*, *16*(10), 1299–1305.

Fu, R., Brey, W. W., Shetty, K., Gor'kov, P., Saha, S., Long, J. R., Grant, S. C., Chekmenev, E. Y., Hu, J., Gan, Z., Sharma, M., Zhang, F., Logan, T. M., Bruschweller, R., Edison, A., Blue, A., Dixon, I. R., Markiewicz, W. D., & Cross, T. A. (2005). Ultra-wide bore 900 MHz high-resolution NMR at the National High Magnetic Field Laboratory. *Journal of Magnetic Resonance*, *177*, 1–8. https://doi.org/10.1016/j.jmr.2005.07.013

Garcia, M. L., Hanner, M., Knaus, H. G., Koch, R., Schmalhofer, W., Slaughter, R. S., & Kaczorowski, G. J. (1997). Pharmacology of potassium channels. *Advances in Pharmacology*, *39*, 425–471.

Garcia-Calvo, M., Leonard, R. J., Novick, J., Stevens, S. P., Schmalhofer, W., Kaczorowski, G. J., & Garcia, M. L. (1993). Purification, characterization, and biosynthesis of margatoxin, a component of *Centruroides margaritatus* venom that selectively inhibits voltage-dependent potassium channels. *Journal of Biological Chemistry*, *268*, 18866–18874.

Goldman, E. R., Mattoussi, H., Anderson, G. P., Medintz, I. L., & Mauro, J. M. (2005). Fluoroimmunoassays using antibody-conjugated quantum dots. *Methods in Molecular Biology*, *303*, 19–34.

Goldman, E. R., Medintz, I. L., Whitley, J. L., Hayhurst, A., Clapp, A. R., Uyeda, H. T., Deschamps, J. R., Lassman, M. E., & Mattoussi, H. (2005). A hybrid quantum dot-antibody fragment fluorescence resonance energy transfer-based TNT sensor. *Journal of the American Chemical Society*, *127*, 6744–6751. https://doi.org/10.1021/ja043677l

Hanson, L. R., & Frey, W. H. (2008). Intranasal delivery bypasses the blood-brain barrier to target therapeutic agents to the central nervous system and treat neurodegenerative disease. *BMC Neuroscience*, *9*(Suppl 3), S5. https://doi.org/10.1186/1471-2202-9-S3-S5

Holmes, T. C., Fadool, D. A., & Levitan, I. B. (1996). Tyrosine phosphorylation of the Kv1.3 potassium channel. *Journal of Neuroscience*, *16*, 1581–1590. https://doi.org/10.1523/JNEUROSCI.16-05-01581.1996

Hwa, J. J., Ghibaudi, L., Williams, P., Witten, M. B., Tedesco, R., & Strader, C. D. (1998). Differential effects of intracerebroventricular glucagon-like peptide-1 on feeding and energy expenditure regulation. *Peptides*, *19*, 869–875. https://doi.org/10.1016/S0196-9781(98)00033-3

Johnson, B. S., Stevens, S. P., & Williamson, J. M. (1994). Determination of the three-dimensional structure of margatoxin by 1H, 13C, 15N triple-resonance nuclear magnetic resonance spectroscopy. *Biochemistry*, *33*, 15061–15070. https://doi.org/10.1021/bi00254a015

Julliard, A. K., Al, K. D., Fadool, D. A., & Palouzier-Paulignan, B. (2017). Nutrient sensing: Another chemosensitivity of the olfactory system. *Frontiers in Physiology*, *8*, 468. https://doi.org/10.3389/fphys.2017.00468

Khabiri, M., Nikouee, A., Cwiklik, L., Grissmer, S., & Ettrich, R. (2011). Charybdotoxin unbinding from the mKv1.3 potassium channel: A combined computational and experimental study. *The Journal of Physical Chemistry B*, *115*, 11490–11500.

Kleene, S. J. (2008). The electrochemical basis of odor transduction in vertebrate olfactory cilia. *Chemical Senses*, *33*(9), 839–859. https://doi.org/10.1093/chemse/bjn048

Knaus, H. G., Koch, R. O., Eberhart, A., Kaczorowski, G. J., Garcia, M. L., & Slaughter, R. S. (1995). [125I]margatoxin, an extraordinarily high affinity ligand for voltage-gated potassium channels in mammalian brain. *Biochemistry*, *34*(41), 13627–13634. https://doi.org/10.1021/bi00041a043

Kooijman, S., Wang, Y., Parlevliet, E. T., Boon, M. R., Edelschaap, D., Snaterse, G., Pijl, H., Romijn, J. A., & Rensen, P. C. (2015). Central GLP-1 receptor signalling accelerates plasma clearance of triacylglycerol and glucose by activating brown adipose tissue in mice. *Diabetologia*, *58*, 2637–2646. https://doi.org/10.1007/s00125-015-3727-0

Kovach, C. P., Al, K. D., Huang, Z., Chelette, B. M., Fadool, J. M., & Fadool, D. A. (2016). Mitochondrial ultrastructure and glucose signaling pathways attributed to the Kv1.3 ion channel. *Frontiers in Physiology*, *7*, 178. https://doi.org/10.3389/fphys.2016.00178

Krimer, L. S., & Goldman-Rakic, P. S. (1997). An interface holding chamber for anatomical and physiological studies of living brain slices. *Journal of Neuroscience Methods*, *75*, 55–58. https://doi.org/10.1016/S0165-0270(97)02265-6

Kues, W. A., & Wunder, F. (1992). Heterogeneous expression patterns of mammalian potassium channel genes in developing and adult rat brain. *European Journal of Neuroscience*, *4*, 1296–1308.

Kupper, J., Bowlby, M. R., Marom, S., & Levitan, I. B. (1995). Intracellular and extracellular amino acids that influence C-type inactivation and its modulation in a voltage-dependent potassium channel. *Pflugers Archiv. European Journal of Physiology*, *430*(1), 1–11. https://doi.org/10.1007/BF00373833

Leatherdale, C. A., Woo, W.-K., Mikulec, F. V., & Bawendi, M. G. (2002). On the absorption cross section of CdSe nanocrystal quantum dots. *The Journal of Physical Chemistry B*, *106*, 7619–7622. https://doi.org/10.1021/jp025698c

Lusk, G. (1924). Analysis of the oxidation of mixtures of carbohydrates and fat. *The Journal of Biological Chemistry*, *59*, 41–42.

Marks, D. R., & Fadool, D. A. (2007). Post-synaptic density 95 (PSD-95) affects insulin-induced Kv1.3 channel modulation of the olfactory bulb. *Journal of Neurochemistry*, *103*, 1608–1627.

Marks, D. R., Tucker, K., Cavallin, M. A., Mast, T. G., & Fadool, D. A. (2009). Awake intranasal insulin delivery modifies protein complexes and alters memory, anxiety, and olfactory behaviors. *Journal of Neuroscience*, *29*, 6734–6751. https://doi.org/10.1523/JNEUROSCI.1350-09.2009

Marom, S., & Levitan, I. B. (1994). State-dependent inactivation of the Kv3 potassium channel. *Biophysical Journal*, *67*(2), 579–589. https://doi.org/10.1016/S0006-3495(94)80517-X

Mast, T. G., Brann, J. H., & Fadool, D. A. (2010). The TRPC2 channel forms protein-protein interactions with Homer and RTP in the rat vomeronasal organ. *BMC Neuroscience*, *11*, 61. https://doi.org/10.1186/1471-2202-11-61

Mast, T. G., & Fadool, D. A. (2012). Mature and precursor brain-derived neurotrophic factor have individual roles in the mouse olfactory bulb. *PLoS One*, *7*, e31978. https://doi.org/10.1371/journal.pone.0031978

Mattoussi, H., Palui, G., & Na, H. B. (2012). Luminescent quantum dots as platforms for probing in vitro and in vivo biological processes. *Advanced Drug Delivery Reviews*, *64*(2), 138–166. https://doi.org/10.1016/j.addr.2011.09.011

Medintz, I. L., Clapp, A. R., Brunel, F. M., Tiefenbrunn, T., Uyeda, H. T., Chang, E. L., Deschamps, J. R., Dawson, P. E., & Mattoussi, H. (2006). Proteolytic activity monitored by fluorescence resonance energy transfer through quantum-dot-peptide conjugates. *Nature Materials*, *5*, 581–589. https://doi.org/10.1038/nmat1676

Medintz, I. L., Clapp, A. R., Mattoussi, H., Goldman, E. R., Fisher, B., & Mauro, J. M. (2003). Self-assembled nanoscale biosensors based on quantum dot FRET donors. *Nature Materials*, *2*, 630–638.

Medintz, I. L., Konnert, J. H., Clapp, A. R., Stanish, I., Twigg, M. E., Mattoussi, H., Mauro, J. M., & Deschamps, J. R. (2004). A fluorescence resonance energy transfer-derived structure of a quantum dot-protein bioconjugate nanoassembly. *Proceedings of the National Academy of Sciences of the United States of America*, *101*(26), 9612–9617. https://doi.org/10.1073/pnas.0403343101

Medintz, I. L., Mattoussi, H., & Clapp, A. R. (2008). Potential clinical applications of quantum dots. *International Journal of Nanomedicine*, *3*(2), 151–167.

Medintz, I. L., Sapsford, K. E., Clapp, A. R., Pons, T., Higashiya, S., Welch, J. T., & Mattoussi, H. (2006). Designer variable repeat length polypeptides as scaffolds for surface immobilization of quantum dots. *The Journal of Physical Chemistry B*, *110*, 10683–10690. https://doi.org/10.1021/jp060611z

Medintz, I. L., Uyeda, H. T., Goldman, E. R., & Mattoussi, H. (2005). Quantum dot bioconjugates for imaging, labeling and sensing. *Nature Materials*, *4*(6), 435–446.

Mout, R., Moyano, D. F., Rana, S., & Rotello, V. M. (2012). Surface functionalization of nanoparticles for nanomedicine. *Chemical Society Reviews*, *41*, 2539–2544.

Mutlu, A. S., Gao, S. M., Zhang, H., & Wang, M. C. (2020). Olfactory specificity regulates lipid metabolism through neuroendocrine signaling in *Caenorhabditis elegans*. *Nature Communications*, *11*, 1450.

Nikouee, A., Khabiri, M., Grissmer, S., & Ettrich, R. (2012). Charybdotoxin and margatoxin acting on the human voltage-gated potassium channel hKv1.3 and its H399N mutant: An experimental and computational comparison. *The Journal of Physical Chemistry B*, *116*, 5132–5240.

Palouzier-Paulignan, B., Lacroix, M. C., Aime, P., Baly, C., Caillol, M., Congar, P., Julliard, A. K., Tucker, K., & Fadool, D. A. (2012). Olfaction under metabolic influences. *Chemical Senses*, *37*, 769–797. https://doi.org/10.1093/chemse/bjs059

Ramos-Jimenez, A., Hernandez-Torres, R. P., Torres-Duran, P. V., Romero-Gonzalez, J., Mascher, D., Posadas-Romero, C., & Juarez-Oropeza, M. A. (2008). The respiratory exchange ratio is associated with fitness indicators both in trained and untrainedmMen: A possible application for people with reduced exercise tolerance. *Clinical Medicine. Circulatory, Respiratory and Pulmonary Medicine*, *2*, 1–9.

Ranganath, L. R., Beety, J. M., Morgan, L. M., Wright, J. W., Howland, R., & Marks, V. (1996). Attenuated GLP-1 secretion in obesity: Cause or consequence? *Gut*, *38*, 916–919. https://doi.org/10.1136/gut.38.6.916

Riera, C. E., Tsaousidou, E., Halloran, J., Follett, P., Hahn, O., Pereira, M. M. A., Ruud, L. E., Alber, J., Tharp, K., Anderson, C. M., Bronneke, H., Hampel, B., Filho, C. D. M., Stahl, A., Bruning, J. C., & Dillin, A. (2017). The sense of smell impacts metabolic health and obesity. *Cell Metabolism*, *26*, 198–211. https://doi.org/10.1016/j.cmet.2017.06.015

Rosenberg, J. T., Sellgren, K. L., Sachi-Kocher, A., Calixto, B. F., Baird, M. A., Davidson, M. W., Ma, T., & Grant, S. C. (2013). Magnetic resonance contrast and biological effects of intracellular superparamagnetic iron oxides on human mesenchymal stem cells with long-term culture and hypoxic exposure. *Cytotherapy.*, *15*, 307–322. https://doi.org/10.1016/j.jcyt.2012.10.013

Sandoval, D. A., Bagnol, D., Woods, S. C., D'Alessio, D. A., & Seeley, R. J. (2008). Arcuate glucagon-like peptide 1 receptors regulate glucose homeostasis but not food intake. *Diabetes*, *57*, 2046–2054. https://doi.org/10.2337/db07-1824

Sandoval, D., Cota, D., & Seeley, R. J. (2008). The integrative role of CNS fuel-sensing mechanisms in energy balance and glucose regulation. *Annual Review of Physiology*, *70*, 513–535. https://doi.org/10.1146/annurev.physiol.70.120806.095256

Sapsford, K. E., Pons, T., Medintz, I. L., Higashiya, S., Brunel, F. M., Dawson, P. E., & Mattoussi, H. (2007). Kinetics of metal-affinity driven self-assembly between proteins or peptides and CdSe-ZnS quantum dots. *Journal of Physical Chemistry C*, *111*, 11528–11538. https://doi.org/10.1021/jp073550t

Schwartz, A. B., Kapur, A., Wang, W., Huang, Z., Fardone, E., Palui, G., Mattoussi, H., & Fadool, D. A. (2017). Margatoxin-bound quantum dots as a novel inhibitor of the voltage-gated ion channel Kv1.3. *Journal of Neurochemistry*, *140*, 404–420. https://doi.org/10.1111/jnc.13891

Sundberg, R. J., & Martin, R. B. (1974). Interactions of histidine and other imidazole derivatives with transition metal ions in chemical and biological systems. *Chemical Reviews.*, *74*(4), 471–517. https://doi.org/10.1021/cr60290a003

Tang-Christensen, M., Larsen, P. J., Goke, R., Fink-Jensen, A., Jessop, D. S., Moller, M., & Sheikh, S. P. (1996). Central administration of GLP-1-(7–36) amide inhibits food and water intake in rats. *American Journal of Physiology-Regulatory, Integrative and Comparative Physiology*, *271*, R848–R856. https://doi.org/10.1152/ajpregu.1996.271.4.R848

Thiebaud, N., Gribble, F., Reimann, F., Trapp, S., & Fadool, D. A. (2019). A unique olfactory bulb microcircuit driven by neurons expressing the precursor to glucagon-like peptide 1. *Scientific Reports*, *9*(1), 15542–51880. https://doi.org/10.1038/s41598-019-51880-9

Thiebaud, N., Johnson, M. C., Butler, J. L., Bell, G. A., Ferguson, K. L., Fadool, A. R., Fadool, J. C., Gale, A. M., Gale, D. S., & Fadool, D. A. (2014). Hyperlipidemic diet causes loss of olfactory sensory neurons, reduces olfactory discrimination, and disrupts odor-reversal learning. *Journal of Neuroscience*, *34*, 6970–6984. https://doi.org/10.1523/JNEUROSCI.3366-13.2014

Thiebaud, N., Llewellyn-Smith, I., Gribble, F., Reimann, F., Trapp, S., & Fadool, D. A. (2016). The incretin hormone glucagon-like peptide 1 increases mitral cell excitability by decreasing conductance of a voltage-dependent potassium channel. *Journal of Physiology*, *594*, 2607–2628. https://doi.org/10.1113/JP272322

Thorne, R. G., Pronk, G. J., Padmanabhan, V., & Frey, W. H. (2004). Delivery of insulin-like growth factor-I to the rat brain and spinal cord along olfactory and trigeminal pathways following intranasal administration. *Neuroscience*, *127*, 481–496. https://doi.org/10.1016/j.neuroscience.2004.05.029

Tortoriello, D. V., McMinn, J., & Chua, S. C. (2004). Dietary-induced obesity and hypothalamic infertility in female DBA/2J mice. *Endocrinology*, *145*, 1238–1247. https://doi.org/10.1210/en.2003-1406

Tortoriello, D. V., McMinn, J. E., & Chua, S. C. (2007). Increased expression of hypothalamic leptin receptor and adiponectin accompany resistance to dietary-induced obesity and infertility in female C57BL/6J mice. *International Journal of Obesity*, *31*, 395–402. https://doi.org/10.1038/sj.ijo.0803392

Tucker, K., Cavallin, M. A., Jean-Baptiste, P., Biju, K. C., Overton, J. M., Pedarzani, P., & Fadool, D. A. (2010). The olfactory bulb: A metabolic sensor of brain insulin and glucose concentrations via a voltage-gated potassium channel. *Results and Problems in Cell Differentiation*, *52*, 147–157.

Tucker, K., Cavallin, M. A., Overton, J. M., & Fadool, D. A. (2010). Ion channel in the olfactory bulb serves as a metabolic sensor. *Chemical Senses*, Poster *217*, 99.

Tucker, K., Cho, S., Thiebaud, N., Henderson, M. X., & Fadool, D. A. (2013). Glucose sensitivity of mouse olfactory bulb neurons is conveyed by a voltage-gated potassium channel. *The Journal of Physiology*, *591*(10), 2541–2561. https://doi.org/10.1113/jphysiol.2013.254086.

Tucker, K. R., Godbey, S. J., Thiebaud, N., & Fadool, D. A. (2012). Olfactory ability and object memory in three mouse models of varying body weight, metabolic hormones, and adiposity. *Physiology and Behavior*, *107*, 424–432. https://doi.org/10.1016/j.physbeh.2012.09.007

Tucker, K., Overton, J. M., & Fadool, D. A. (2008). Kv1.3 gene-targeted deletion alters longevity and reduces adiposity by increasing locomotion and metabolism in melanocortin-4 receptor-null mice. *International Journal of Obesity*, *32*, 1222–1232. https://doi.org/10.1038/ijo.2008.77

Tucker, K., Overton, J. M., & Fadool, D. A. (2012). Diet-induced obesity resistance of Kv1.3-/- mice is olfactory bulb dependent. *Journal of Neuroendocrinology*, *24*, 1087–1095. https://doi.org/10.1111/j.1365-2826.2012.02314.x

Upadhyay, S. K., Eckel-Mahan, K. L., Mirbolooki, M. R., Tjong, I., Griffey, S. M., Schmunk, G., Koehne, A., Halbout, B., Iadonato, S., Pedersen, B., Borrelli, E., Wang, P. H., Mukherjee, J., Sassone-Corsi, P., & Chandy, K. G. (2013). Selective Kv1.3 channel blocker as therapeutic for obesity and insulin resistance. *Proceedings of the National Academy of Sciences of the United States of America*, *110*, E2239–E2248.

Wang, W., Ji, X., Burns, H., & Mattoussi, H. (2016). A multi-coordinating polymer ligand optimized for the functionalization of metallic nanocrystals and nanorods. *Faraday Discussions*, *191*, 481–494. https://doi.org/10.1039/C6FD00056H

Wang, W., Ji, X., Du, L., & Mattoussi, H. (2007). Enhanced colloidal stability of various gold nanostructures wsing a multicoordinating polymer coating. *Journal of Physical Chemistry C*, *121*(41), 22901–22913.

Wang, W., Ji, X., Kapur, A., Zhang, C., & Mattoussi, H. (2015). A multifunctional polymer combining the imidazole and zwitterion motifs as a biocompatible compact coating for quantum dots. *Journal of the American Chemical Society*, *137*(44), 14158–14172. https://doi.org/10.1021/jacs.5b08915

Wang, W., Kapur, A., Ji, X., Zeng, B., Mishra, D., & Mattoussi, H. (2016). Multifunctional and high affinity polymer ligand that provides bio-orthogonal coating of quantum dots. *Bioconjugate Chemistry*, *27*(9), 2024–2036. https://doi.org/10.1021/acs.bioconjchem.6b00309

Xu, J., Koni, P. A., Wang, P., Li, G., Kaczmarek, L. K., Wu, Y., Li, Y., Flavell, R. A., & Desir, G. V. (2003). The voltage-gated potassium channel Kv1.3 regulates energy homeostasis and body weight. *Human Molecular Genetics*, *12*, 551–559.

Yu, K., Fu, W., Liu, H., Luo, X., Chen, K. X., Ding, J., Shen, J., & Jiang, H. (2004). Computational simulations of interactions of scorpion toxins with the voltage-gated potassium ion channel. *Biophysical Journal*, *86*, 3542–3555. https://doi.org/10.1529/biophysj.103.039461

Yu, W. W., & Peng, X. (2002). Formation of high-quality CdS and other II-VI semiconductor nanocrystals in noncoordinating solvents: Tunable reactivity of monomers. *Angewandte Chemie (International Ed. in English)*, *41*, 2368–2371.

Zhan, N., Palui, G., Safi, M., Ji, X., & Mattoussi, H. (2013). Multidentate zwitterionic ligands provide compact and highly biocompatible quantum dots. *Journal of the American Chemical Society*, *135*, 13786–13795.

SUPPORTING INFORMATION

Additional supporting information may be found online in the Supporting Information section.

How to cite this article: Schwartz AB, Kapur A, Huang Z, et al. Olfactory bulb-targeted quantum dot (QD) bioconjugate and Kv1.3 blocking peptide improve metabolic health in obese male mice. *J. Neurochem.* 2020;00:1–21. https://doi.org/10.1111/jnc.15200